Energy Reports 8 (2022) 860–877

Contents lists available at ScienceDirect

Energy Reports

journal homepage: www.elsevier.com/locate/egyr

Research paper

# Optimal design of controllers and harmonic compensators for three-level cascaded control in stationary reference frame for grid-supporting inverters-based AC microgrid

Mohamed A. Ebrahim [a], Beshoy Abdou Aziz [b,*], Maged N.F. Nashed [c], F.A. Osman [b]

[a] Faculty of Engineering at Shoubra, Benha University, Shoubra, Cairo, Egypt
[b] Benha Faculty of Engineering, Benha University, Qalubia, Egypt
[c] Power Electronics and Energy Conversion Department, Electronics Research Institute, Cairo, Egypt

ARTICLE INFO

*Article history:*
Received 29 June 2021
Received in revised form 13 November 2021
Accepted 22 November 2021
Available online xxxx

*Keywords:*
Hierarchical control
Harmonic compensators
Microgrids
Optimization techniques
Power quality
Proportional-resonant controller

ABSTRACT

In this paper, new optimal procedures are introduced to design the finest controllers and harmonic compensators (HCs) of three-level cascaded control for three-phase grid-supporting inverters based-AC microgrid. The three control levels, comprising primary, secondary and synchronization control levels, are developed in stationary $\alpha\beta$-frame and based on the proportional–integral (PI) controllers and the proportional-resonant controllers along with additional HCs. The new optimal design guidelines of microgrid's controllers and HCs are aimed to fulfill the study requirements. The optimization objectives and constraints are employed to minimize both the total harmonic distortion (THD) and individual harmonics of microgrid's voltage to enhance the quality of microgrid's output power. The THD of microgrid's voltage can be reduced to 0.19% under the nonlinear loads. Moreover, the microgrid's voltage and frequency can be perfectly regulated with zero deviations. Furthermore, these new optimal procedures accelerate the speed of synchronization process between the external power grid and the microgrid to be accomplished in time less than 20 ms. Additionally, an accurate power-sharing among paralleled operated inverters can be achieved to avoid overstressing on any one. Also, seamless transitions can be guaranteed between grid-tied and isolated operation mode. The optimal controllers and HCs are designed by a new optimization algorithm called H-HHOPSO, which is created by hybridizing between Harris hawks optimization and particle swarm optimization algorithms. The effectiveness and robustness of the H-HHOPSO-based controllers and HCs are compared with other meta-heuristic optimization algorithms-based controllers and HCs. A microgrid, including two grid-supporting inverters based optimal controllers and optimal HCs, are modeled and carried out using MATLAB/SIMULINK to test the performance under linear and nonlinear loads, and also during the interruption of any one of two inverters. The performance is investigated according to IEC/IEEE harmonic standards, and compared with the conventional control strategy developed in synchronous *dq*-frame and based on only PI controllers.



## 1. Introduction

Recently, the shortage of fossil fuel resources and the increase of greenhouse gas emissions have motivated researchers to use renewable energy resources (RERs) to alleviate the energy crisis and overcome environmental and economic issues (Andishgar et al., 2017; Meng et al., 2019). The distributed energy resources (DERs), including RERs and energy storage elements (ESEs), can be grouped as a locally controllable microgrid in the main power grid to supply the electrical power with minimum losses to the local loads (Farrokhabadi et al., 2020). These DERs can be interfaced with the main power grid and local loads through either a conventional synchronous generator or power electronic converter. The grid-supporting voltage source inverters (VSIs) in AC microgrids are the most significant part which is able not only to harmonious operate in parallel with each other but also has high flexibility to connect or disconnect from the external power grid (Guo and Mu, 2016).

A high penetration level of converters-interfaced RERs into microgrids causes several challenges to the stability and operation of power systems due to the intermittent nature and uncertainties of RERs. Therefore, appropriate microgrid architectures and control approaches for VSIs based-DERs are essential to enhance the quality of output power and guarantee the efficiency, reliability, safety and stability of power systems (Zhou and Ngai-Man Ho, 2016). Many hierarchical control architectures have been addressed in Guerrero et al. (2011, 2013) and Bidram and Davoudi

* Corresponding author.
*E-mail address:* beshoy.abdo@bhit.bu.edu.eg (B.A. Aziz).

https://doi.org/10.1016/j.egyr.2021.11.248

**Nomenclature**

| | |
|---|---|
| DERs | Renewable energy resources |
| DG | Distribution generation |
| ESEs | Energy storage elements |
| FF | Fitness function |
| HCs | Harmonic compensators |
| ITAE | Integral time absolute error |
| LF | Levy flight |
| PCL | Primary control level |
| PI | Proportional–integral |
| PR | Proportional-resonant |
| RERs | Renewable energy resources |
| SCL | Secondary control level |
| TCL | Tertiary control level |
| THD | Total harmonic distortion |
| VSIs | Voltage source inverters |
| $C_1$, $C_2$, $C_3$, $C_4$, $C_5$, $C_6$, $C_8$, $C_9$, $q$, $r$ | Random coefficients which are often in the range [0–1] and updated in each iteration |
| $C_7$ | Random vector with dimension 1 × d |
| $d$ | Dimension of variables |
| $E_0$ | Initial value of escaping energy of the rabbit |
| $E_{pry}$ | Escaping energy of the prey |
| $e_P$, $e_Q$ | Errors in active and reactive powers of droop control |
| $e_{secf}$, $e_{secE}$ | Errors in frequency and voltage amplitude of SCL |
| $e_{syn\theta}$, $e_{synE}$ | Errors in phase angle and voltage amplitude of synchronization control level |
| $e_{V\alpha}$, $e_{V\beta}$, $e_{I\alpha}$, $e_{I\beta}$ | Errors of voltage and current in $\alpha$- and $\beta$-axis |
| $G(s)$, $Z_{o\alpha\beta}$ | Closed-loop transfer function of voltage and output impedance of inverter in $\alpha\beta$-frame |
| $I_{o\alpha\beta}$ | Output currents in $\alpha\beta$-frame |
| J | Random jump strength of the prey during the escaping behavior |
| $K$ | Total hawks number |
| $K_{hI}$, $\omega_{chI}$, $K_{hV}$, $\omega_{chV}$ | Resonant gain and cut-off frequency around resonant-frequency h$\omega_o$ of current and voltage HCs for harmonic order h |
| $K_{pDP}$, $K_{iDP}$ | Proportional and integral droop coefficients for active power control |
| $K_{pDQ}$ | Proportional droop coefficient for reactive power control |
| $K_{pI}$, $K_{rI}$, $\omega_{cI}$, $K_{pV}$, $K_{rV}$, $\omega_{cV}$ | Proportional gain, resonant gain and cut-off frequency around fundamental-frequency $\omega_o$ of PR current and voltage controllers |
| $K_{psf}$, $K_{isf}$, $K_{psE}$, $K_{isf}$ | Proportional and integral gains of frequency and voltage amplitude secondary PI controllers |
| $K_{p\theta}^{syn}$, $K_{i\theta}^{syn}$, $K_{pE}^{syn}$, $K_{iE}^{syn}$ | Proportional and integral gains of frequency and voltage amplitude PI synchronization controllers |
| $LB$, $UB$ | Lower and upper bounds of optimization problem variables |
| $L_f$, $R_f$ | Inductance and capacitance of LC-filter |
| $M$ | Maximum number of iterations |
| $P$, $Q$, $P^*$, $Q^*$ | Active and reactive powers, and their references |
| $R_{vir}$, $L_{vir}$ | Resistance and inductance of the virtual impedance |
| $T_{sa}$ | Sampling time |
| $V^*$, $\varnothing^*$, $V_r$, $\varnothing_r$ | Reference and nominal values of the voltage amplitude and its phase angle |
| $v(t)$ | Current velocity of particle in PSO |
| $v\ (t+1)$ | Updated velocity of particle in PSO |
| $V_{cf\alpha}$, $V_{cf\beta}$, $i_{Lf\alpha}$, $i_{Lf\beta}$ | Voltage across filter capacitor and current through filter inductor in $\alpha$- and $\beta$-axis |
| $V_{cf\alpha\beta}$, $V^*_{c\alpha\beta}\ (s)$ | Voltages across the filter capacitor in $\alpha\beta$-frame and their references |
| $V_{oi}$, $V_{bus}$ | Amplitude of the VSI output voltage and the amplitude of network bus voltage |
| $v_{MG\alpha}$, $v_{MG\beta}$, $v_{EG\alpha}$, $v_{EG\beta}$ | Microgrid and external grid voltages in $\alpha$- and $\beta$-axis |
| $V_{vir\alpha}$, $V_{vir\beta}$ | Voltage correction signal of virtual impedance loop in $\alpha$-and $\beta$-axis |
| $X(t)$ | Current positions of hawks |
| $X(t+1)$ | Updated positions of hawks in the next iteration t |
| $X_{av}(t)$ | Average location of the current hawks population |
| $X_{dl}$ | Reactance of distribution line |
| $X_i(t)$ | The hawk i position in iteration $t$ |
| $X_{pry}(t)$ | Position of the prey |
| $X_{rnd}\ (t)$ | Hawk position which is selected randomly from the current population |
| $Z_{vir\alpha\beta}$ | Virtual impedance in $\alpha\beta$-frame |
| $\propto_1$, $\propto_2$ | Priority weights for terms in the proposed multi-objective function |
| $\beta\ (t)$ | PSO time-varying inertia weight |
| $\beta_{max}$, $\beta_{min}$ | Maximum and minimum inertia weights of PSO algorithm |
| $\gamma$ | Constant adjust to 1.5 |
| $\delta\omega_{sec}^{comp}$, $\delta E_{sec}^{comp}$ | Compensation signals of SCL |
| $\Delta\theta_{syn}$, $\Delta E_{syn}$ | Compensation signals of synchronization control level |
| $\varnothing$ | Angle between $V_{bus}$ and $V_{oi}$, which is called the load angle |
| $\omega_{cL}$ | Cut-off frequency of the low pass filter |
| $\omega_o$ | Fundamental angular frequency of the microgrid |
| $\omega_{MG}^*$, $\omega_{MG}^{meas}$, $E_{MG}^*$, $E_{MG}^{meas}$ | Reference and measured values of angular frequency and voltage amplitude |

(2012) to make the grid-supporting VSIs-based microgrid capable of working in both isolated and grid-connected modes of operation. This hierarchical control has three control levels comprising of primary control level (PCL), secondary control level (SCL) and tertiary control level (TCL). The PCL is applied locally at each distribution generation (DG) unit to achieve its responsibilities represented in the regulation and stabilization of the frequency and voltage, a realization of accurate power-sharing

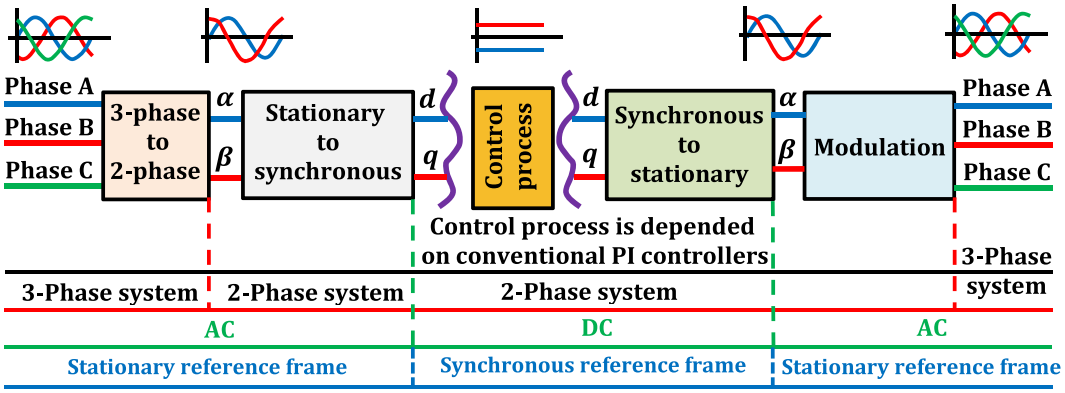


(a) Conventional control strategy developed in synchronous $dq$ reference frame

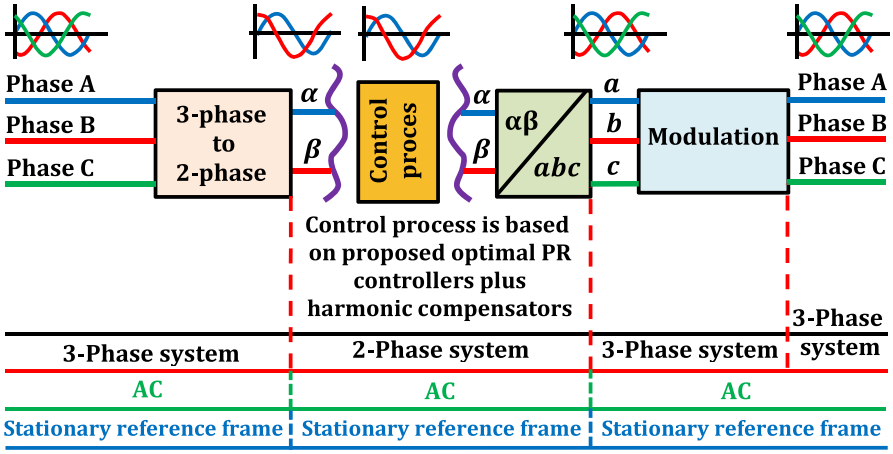


(b) Control approach developed in stationary $\alpha\beta$ frame and based on the proposed optimal PR controllers and HCs

**Fig. 1.** Two control methodologies developed in different reference frames.

among paralleled DG units via droop control strategy, and enhancement of output power quality. Another level of control is needed for remedying the drawback of the droop control technique which makes the voltage and frequency to deviate from their nominal values. Therefore, the centralized SCL is responsible for nullifying these deviations created by droop loops in PCL for restoring the frequency and voltage to their nominal values. Moreover, the synchronization process between the external main grid and the microgrid is achieved through the SCL. The TCL is the upper centralized layer of control required to optimize the microgrid's operational cost, and also to manage the power flow in grid-connected mode from the microgrid to the external power grid, and vice versa (Shrivastava et al., 2018).

Due to the unbalanced and nonlinear loads involved in the microgrids, the power quality issues are produced in the form of voltage/frequency deviations and fluctuations, current and voltage distortions, power variations, flickers, and voltage swell/sag. The microgrid entity is capable of dealing with these power quality issues using proper control techniques to meet acceptable standards. In the literature, the existing methodologies for power quality enhancement vary significantly including multiple current-loop active damping schemes-based hierarchical control architecture (Han et al., 2017), voltage harmonic compensation using active power filter and coordinated control of DERs VSIs (Hashempour et al., 2016), resonance damping and control of DERs converters (Li, 2009), voltage harmonic reduction for inverters using harmonic droop controller (Zhong, 2013), hybrid voltage/current control technique for grid-interfaced DERs converters (He and Li, 2013), and compensation and sharing of nonlinear and unbalanced loads (Yazdavar et al., 2019; Golsorkhi et al., 2017; Sreekumar and Khadkikar, 2016; He et al., 2015). In Han et al. (2017), the total harmonic distortion (THD) of inverter's output voltage under nonlinear load reduced from 5.45% in the case of without harmonic loops compensation to 1.2% in the case of adding the proposed harmonic loops compensation. The authors of Vasquez et al. (2013) suggested a PCL based on proportional-resonant (PR) controller along with additional harmonic compensators (HCs) in stationary $\alpha\beta$-frame to suppress the inverter's output voltage harmonics generated by nonlinear loads. In this reference, the THD of the inverter's output voltage under nonlinear load decreased from 5.61% in the case of deactivating HCs loops to 0.63% in the case of activating HCs loops. T.K. Vu, S.J. Seong presented a comparative study of proportional–integral (PI) and PR controller for single-phase grid-interfaced inverter system (Vu and Seong, 2010). The simulation results concluded that the current THD reduced from 10.32% for PI controller to 6.73% for PR controller. Other previous research works have focused on the voltage and frequency regulation in AC and DC microgrids for uncertain stochastic nonlinear system with application to energy Internet. A non-fragile robust $H_\infty$ control methodology was employed in Hua et al. (2018) for isolated DC microgrids to regulate intelligently the deviation of DC bus voltage within an Internet energy scenario. In Hua et al. (2020), a mixed $H_2/H_\infty$ control approach with Markov chains was introduced and used for AC microgrids to share the energy and regulate the frequency in Internet energy.

In the literature, most of the control approaches for AC microgrids are developed in either stationary $\alpha\beta$ reference frame or synchronous $dq$ reference frame. Fig. 1a shows the conventional control strategy developed in $dq$ reference frame. It can

be observed that the three-phase voltages and currents are converted from three-phase time-variant quantities (i.e., $x_a$, $x_b$ and $x_c$) to two-phase time-variant quantities (i.e., $x_\alpha$ and $x_\beta$) using Clarke transformation matrix. Then, the two-phase time variant quantities are converted to two-phase time-invariant quantities (i.e., $x_d$ and $x_q$) using Park transformation matrix. The control laws are carried out under synchronous dq reference frame using the conventional PI controllers. The obtained references of dq voltages must be converted back to $\alpha\beta$ voltages for space vector pulse width modulation or abc voltages for sinusoidal pulse width modulation. This can be achieved using the inverse matrices of Clarke and Park. The transformation matrices between the reference frames can be found in Shuvo et al. (2020). Fig. 1b presents the control approach based on the proposed optimal PR controllers with their HCs. It can be noticed that the control laws are carried out under stationary $\alpha\beta$ reference frame without needing $\alpha\beta -$ to $- dq$ transformations and vice versa. In contrast to the conventional control strategy developed in synchronous $dq$ frame and based on PI controllers, the control approach developed in $\alpha\beta$ frame and based on PR controllers has a superior performance in tracking a sinusoidal waveform reference without steady-state error and also has a high capability in disturbance rejection (Gui et al., 2018). Moreover, the PR controllers can be integrated along with their HCs to suppress the selective negative and positive harmonics. Due to the control techniques based on PR controllers and their HCs are developed in stationary $\alpha\beta$-frame instead of synchronous dq-frame as in PI controllers-based control approaches, no feed-forward parts and no decoupling terms are required (Vasquez et al., 2013). Consequently, the optimal control approach in this work is developed in stationary $\alpha\beta$-frame and based on PR controllers along with their additional HCs. The major challenge to using these PR controllers with additional HCs is how to design their many parameters to achieve the control objectives and enhance the power quality. The existing design procedures of PR controllers and their HCs in Han et al. (2017), Vasquez et al. (2013), Gui et al. (2018) and Zammit et al. (2017) are based on the trial-error method, root-locus plots, bode plots and MATLAB's SISO Design Tool. These conventional design methods are inaccurate and ineffective procedures and consume more time. Subsequently, the vision of this article is to introduce artificial intelligence (AI) algorithms-based new optimal design procedures of PR controllers and HCs for control schemes applied to grid-supporting VSIs-based microgrids. In contrast to the previous studies in the same research area mentioned in this paper, our proposed optimal PR controllers and HCs have a superior performance and better results. Unlike the adaptive PI controller which is suggested in Elnady and AlShabi (2019) for microgrid under balanced loads where the microgrids's voltage THD was 1.6%, our proposed optimal PR controllers and HCs under nonlinear loads can reduce the THD to 0.19%. Moreover, a comparison between various types of controllers, including conventional PI, PI plus HCs, and PI-P plus HCs, has been done for isolated microgrids under nonlinear load in Ortega Gonzalez et al. (2014). The microgrid's voltage THD values are found to be 8.8% for conventional PI, 5.2% for PI plus HCs, and 2.2% for PI-P plus HCs. This implies that the suggested optimal PR controllers and HCs in this study are more effective and efficient than those mentioned in the previous research works.

Previous research works focused on employing AI algorithms in the microgrids to select the optimal parameters of PI controllers. In Ebrahim et al. (2021), a novel hybrid algorithm, namely H-HHOPSO, is implemented by hybridization between Harries hawks optimization (HHO) and particle swarm optimization (PSO) algorithms. This reference applied H-HHOPSO algorithm on the new microgrid architecture to optimize the PI controllers' parameters of four control levels. The authors of Jumani et al. (2018) employed the grasshopper optimization algorithm to find the best PI controllers' gains for one control level-based islanded microgrid. M. A. Ebrahim, et al. used a self-adaptive salp swarm optimization algorithm in an isolated microgrid for choosing its PI controllers' coefficients (Ebrahim et al., 2020). In contrast to the PI controllers, the design of PR controllers and their HCs is insufficiently studied in the literatures. In yan Jiang et al. (2020), an optimal PR controller without any HCs is designed by using PSO algorithm for AC microgrid. In Gao et al. (2020), only the resonant term of PR controller was designed and used as active damping approach for grid-connected inverters. To the best of the authors' knowledge, no previous research works employ the AI algorithms in AC microgrids to design optimally the coefficients of PR controllers with their HCs.

The main contributions of the research work introduced in this article can be summarized as follows

- New design guidelines, based on the new H-HHOPSO algorithm cooperated with new proposed multi-objective functions, are presented for tackling one of the most popular microgrid technical issues represented in the optimal parameter-tuning of its controllers and HCs. In this paper, the optimal control approach has three levels of control developed in stationary $\alpha\beta$-frame, including PCL, SCL and synchronization control level, based on PR controllers along with additional HCs and PI controllers. New formulations are developed for optimization problem of three-level control-based microgrid. The optimization problem of three-level control-based microgrid is formulated. The optimal design procedures are carried out throughout two stages. The first stage is employed for the PCL to optimize its voltage/current PR controllers with additional HCs to regulate perfectly both the voltage and frequency and also to suppress the fifth, seventh, eleventh and thirteenth harmonics in microgrid's output voltage under linear and nonlinear loads. The second stage is used to get the best droop controller's coefficients, and also to optimize the voltage and frequency PI controllers for SCL and synchronization control level. The proposed multi-objective function in the second stage is aimed to eliminate the differences in voltage amplitude, frequency and phase angle between the microgrid and the external power grid, and also to achieve accurate power-sharing among paralleled operated grid-supporting inverters.
- A solid comparative study is done among the conventional PI controllers in synchronous dq-frame, other controllers introduced in the literatures, the proposed H-HHOPSO-based PR controllers and HCs in stationary $\alpha\beta$-frame and other meta-heuristic optimization algorithms-based PR controllers with additional HCs in stationary $\alpha\beta$-frame. This comparative study is to prove and confirm the robustness of the proposed optimal controllers and HCs.

The organizational structure of the rest of the paper is as follows: mathematical modeling of the H-HHOPSO optimization algorithm is expressed in Section 2. Section 3 introduces the PCL methodology for grid-supporting VSIs, while the SCL and synchronization control level are described in Section 4. Section 5 presents the proposed optimal design procedures of microgrid's controllers and HCs. The simulation results with a comparative study between various types of microgrid's controllers and HCs are introduced and discussed in Section 6. Finally, the work done in this article can be concluded in Section 7.

## 2. H-HHOPSO optimization algorithm

The H-HHOPSO is created by hybridizing between HHO and PSO algorithms. The strength of PSO in exploration is synthesized

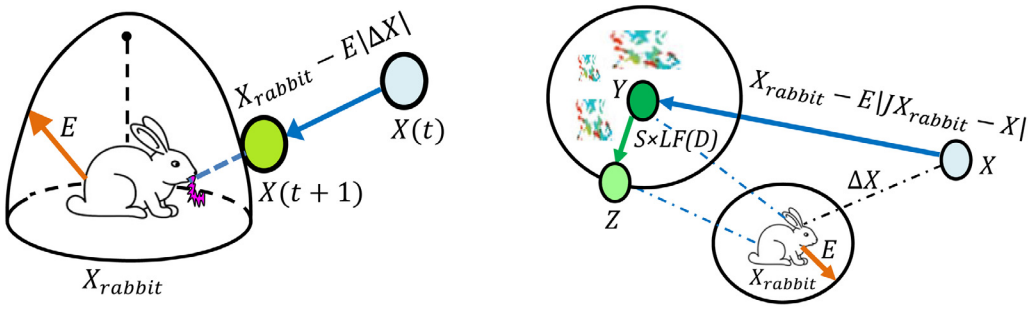


(a) Hard besiege (b) Soft besiege

**Fig. 2.** Two main strategies of Harries hawks.

with the strength of HHO in exploitation to get a more efficient and effective algorithm. The PSO algorithm was introduced in Kennedy and Eberhart (1995) and inspired by nature from the social behavior of birds and fishes swarms in seeking food. Recently, a new algorithm called HHO has been suggested in Heidari et al. (2019) and nature-inspired by the cooperative behavior and attacking mechanism of Harris hawks to grasp the prey (rabbit). The Harries hawks change their positions for catching the prey according to two main strategies, namely hard and soft besiege strategy. The hard besiege strategy is shown in Fig. 2a. In this strategy, the hawks will change their positions from $X(t)$ to $X(t+1)$ and catch the rabbit. The soft besiege strategy is depicted in Fig. 2b. In this strategy, the hawks are having a lesser chance to grasp the rabbit and therefore they will change their locations to the next possible positions $Y$ or $Z$ and will try to grasp the rabbit from location Y or location $Z$ using the strategy of Levy Flight (LF).

The H-HHOPSO is a novel hybrid algorithm presented in Ebrahim et al. (2021). This algorithm combines the advantages of both HHO and PSO algorithms, hence gives a balance for both the exploitation and exploration performance to achieve the best solutions. The effectiveness of H-HHOPSO algorithm has been confirmed in Ebrahim et al. (2021) through using it to solve twenty-three well-known benchmark problems with different dimensions and ranges. The mathematical model of H-HHOPSO algorithm can be represented as follows: Firstly, the Harris hawks are in the phase of exploration and the prey's escaping energy $|E_{pry}|$ is greater than or equal one, in which the hawks roost randomly on some positions and use two mechanisms to detect a rabbit. The two mechanisms are modeled as the following (Ebrahim et al., 2021)

$$\begin{cases} X(t+1) = \beta(t) * (X_{md}(t) \\ \quad -C_1 |X_{md}(t) - 2C_2 X(t)|) & q \geq 0.5 \\ X(t+1) = \beta(t) * \left(X_{pry}(t) - X_{av}(t)\right) \\ \quad -C_3 (LB + C_4 (UB - LB)) & q < 0.5 \end{cases} \tag{1}$$

$$v(t+1) = \beta(t) * \left(v(t) + C_5 * \left(X(t+1) - X_{pry}(t)\right)\right) \tag{2}$$

$$X(t+1) = X(t+1) + v(t+1) \tag{3}$$

where,

$$E_{pry} = 2E_0 (1 - t/M) \tag{4}$$

$$\beta(t) = \beta_{max} - ((\beta_{max} - \beta_{min}) * t/\mathrm{M}) \tag{5}$$

$$X_{av}(t) = 1/K \sum_{i=1}^{K} X_i(t) \tag{6}$$

Here, $X(t+1)$ are the new locations of hawks after one iteration $t$; $X(t)$ are the current locations of Harris' hawks; $X_{pry}(t)$ is the prey location; $X_{rnd}$ is the hawk location, which is selected randomly from the current population; $\beta(t)$ is the time-varying inertia weight of PSO; $\beta_{min}$ and $\beta_{max}$ are the minimum and maximum PSO inertia weights, which equal 0.2 and 0.9, respectively; UB and LB are the upper bound and lower bound of variables; $C_1$, $C_2$, $C_3$, $C_4$, $C_5$ and $q$ are coefficients varied randomly from 0 to 1 and updated in each iteration $t$; M is the maximum iteration number; $X_{av}(t)$ is the average location of the current hawks population; $K$ is the total hawks number; $X_i(t)$ is the hawk i position in iteration $t$; $v(t+1)$ is the updated velocity of PSO particle; $E_0$ is the initial prey's escaping energy and $M$ is the maximum number of iterations.

Secondly, the Harris hawks are transferred from the exploration to exploitation phase and the prey's escaping energy $|E_{pry}|$ is less than one. In this situation, the hawks attack the prey using four strategies based on the value of the prey's escaping energy and a random variable of $r$. The updated positions of hawks in the exploitation phase are represented as the following (Ebrahim et al., 2021)

$$X(t+1) = \begin{cases} X_1 & if \ |E_{pry}| < 0.5 \ and \ r \geq 0.5 \\ X_2 & if \ |E_{pry}| \geq 0.5 \ and \ r \geq 0.5 \\ X_3 & if \ |E_{pry}| \geq 0.5, r < 0.5 \ and \ F(X_3) < F(X(t)) \\ X_4 & if \ |E_{pry}| \geq 0.5, r < 0.5 \ and \ F(X_4) < F(X(t)) \\ X_5 & if \ |E_{pry}| < 0.5, r < 0.5 \ and \ F(X_5) < F(X(t)) \\ X_6 & if \ |E_{pry}| < 0.5, r < 0.5 \ and \ F(X_6) < F(X(t)) \end{cases} \tag{7}$$

$$v(t+1) = \alpha(t) * \left(v(t) + C_5 * \left(X(t+1) - X_{pry}(t)\right)\right) \tag{8}$$

$$X(t+1) = X(t+1) + v(t+1) \tag{9}$$

where

$$X_1 = \beta(t) * \left(X_{pry}(t) - E_{pry} \left|X_{pry}(t) - X(t)\right|\right) \tag{10}$$

$$X_2 = \beta(t) * \left(X_{pry}(t) - X(t)\right) - E_{pry} \left|JX_{pry}(t) - X(t)\right| \tag{11}$$

$$X_3 = \beta(t) * \left(X_{pry}(t) - E_{pry} \left|JX_{pry}(t) - X(t)\right|\right) \tag{12}$$

$$X_4 = \beta(t) * \left(\frac{X_3}{\beta(t)} + C_7 * LF(d)\right) \tag{13}$$

$$X_5 = \beta(t) * \left(X_{pry}(t) - E_{pry} \left|X_{pry}(t) - X_{av}(t)\right|\right) \tag{14}$$

$$X_6 = \beta(t) * \left(\frac{X_5}{\beta(k)} + C_7 * LF(d)\right) \tag{15}$$

$$J = 2(1 - C_6) \tag{16}$$

$$LF(x) = 0.01 * C_8 * \mu / |C_9|^{1/\gamma} \tag{17}$$

$$\mu = \left(\frac{\Gamma(1+\gamma) * sin(\pi\gamma/2)}{\Gamma((1+\gamma)/2) * \gamma * 2^{(\gamma-1)/2}}\right)^{1/\gamma} \tag{18}$$

Here, $C_6$, $C_8$, $r$, and $C_9$ are random coefficients in the range [0–1]; $LF(x)$ is the levy-flight function; $d$ is the dimension of the variables; $C_7$ is a random vector by length $1 \times$ d; $\gamma$ is a constant

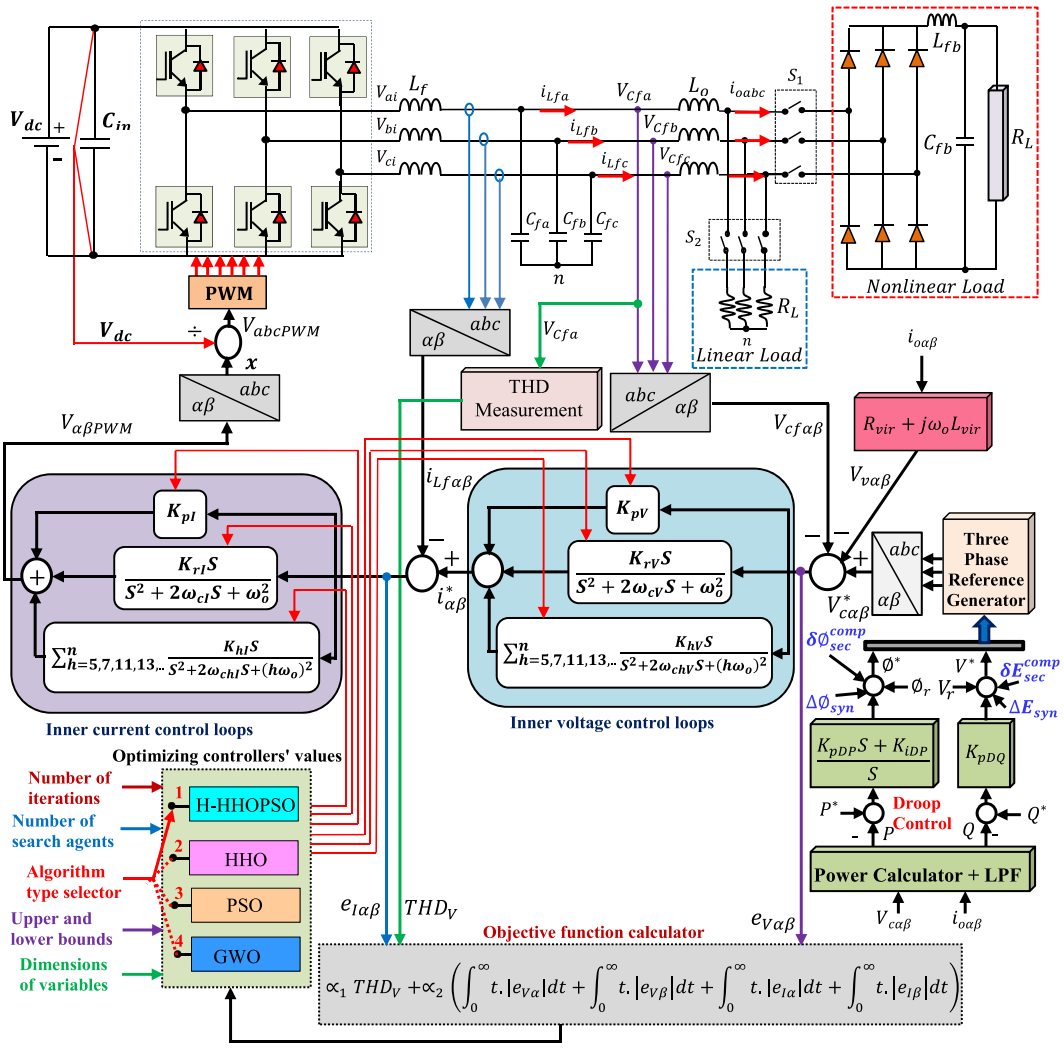


**Fig. 3.** Proposed primary control strategy for grid-supporting VSIs developed in stationary $\alpha\beta$-frame and based on optimal current/voltage PR controllers and their HCs.

of 1.5; and $J$ is the strength of the prey's random jump which mimics the prey's escaping behavior.

## 3. Primary control of grid-supporting VSIs

Fig. 3 describes the power stage of a grid-supporting VSI and its proposed primary control methodology developed in stationary $\alpha\beta$-frame and based on optimal droop controllers as well as optimal current/voltage PR controllers along with their additional HCs. The power stage comprises a three-phase pulse width modulation inverter and an LC-filter with an additional output inductor. The PCL approach for grid-supporting inverter, presented in Fig. 3, consists of eight feedback loops of control (1) four inner current and voltage control loops for regulating properly the $\alpha\beta$-axis currents and voltages $i_{Lf\alpha}$, $i_{Lf\beta}$, $V_{cf\alpha}$ and $V_{cf\beta}$, respectively (2) two outer active/reactive power loops (i.e., droop control loops) for realizing accurate active/reactive power-sharing among the paralleled grid-supporting VSIs (3) two intermediate virtual impedance loops for controlling the output impedance of grid-supporting inverter.

### 3.1. Inner voltage and current control loops

As illustrated in Fig. 3, the voltage controllers track the reference signals produced by active/reactive power controllers and generate the references for the current controllers. The current controllers' output is transformed from stationary $\alpha\beta$-frame to stationary abc-frame and then divided by a dc-link voltage to obtain the three-phase voltage references for the PWM. The inner voltage and current control loops are based on the PR controllers along with HCs to overcome the difficulties of using PI controllers to follow AC signals. The PR controllers have a superior performance in following the current and voltage signals in stationary $\alpha\beta$-frame without any steady-state error. The PR controller includes a proportional term plus a resonant term tuned at the fundamental frequency. The HCs can be included with the PR controller for selective harmonics compensation. In this paper, there are four HCs for both current and voltage PR controllers to suppress the 5th, 7th, 11th and 13th microgrid's voltage harmonics generated by nonlinear loads. Each harmonic compensator includes only a resonant term which is tuned at the frequency of the selective harmonic order.

The dynamics of the closed-loop system, shown in Fig. 4, can be analyzed as follows

$$V_{cf\alpha\beta}(s) = G(s)V^{*}_{c\alpha\beta}(s) - I_{o\alpha\beta}(s)Z_{o\alpha\beta}(s) - G(s)Z_{vir\alpha\beta}(s) \tag{19}$$

where

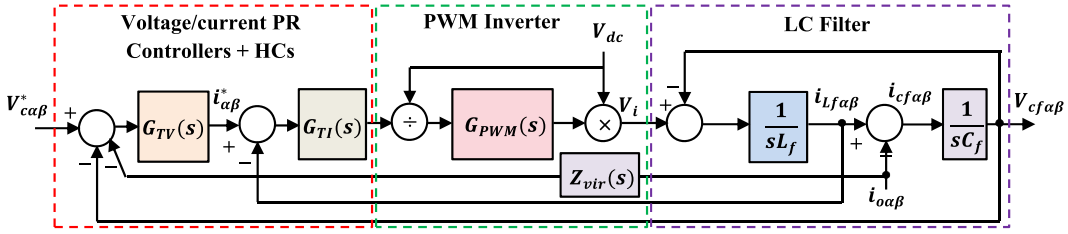


**Fig. 4.** Block diagram of the closed loops for grid-supporting VSIs based on PR controllers with HCs.

The closed-loop transfer function of the microgrid's output voltage can be derived as

$$G(s) = \frac{G_{TV}(s)G_{TI}G_{PWM}(s)}{L_f C_f S^2 + \left(C_f S + G_{TV}(s)\right) G_{TI}G_{PWM}(s) + 1} \tag{20}$$

The transfer function of the output impedance is expressed as

$$Z_{o\alpha\beta}(s) = \frac{L_f S + G_{TI}(s)G_{PWM}(s)}{L_f C_f S^2 + \left(C_f S + G_{TV}(s)\right) G_{TI}(s)G_{PWM}(s) + 1} \tag{21}$$

Here, $V_{cf\alpha\beta}$ and $V^*_{c\alpha\beta}$ $(s)$ are the voltages across the filter capacitor in $\alpha\beta$-frame and their references, respectively; $I_{o\alpha\beta}$ are the output currents in $\alpha\beta$-frame; $G(s)$ and $Z_{o\alpha\beta}$ are the closed-loop transfer function of voltage and output impedance of inverter in $\alpha\beta$-frame, respectively; $L_f$ and $C_f$ are the inductance and capacitance of LC-filter, respectively; and $Z_{vir\alpha\beta}$ is the virtual impedance in $\alpha\beta$-frame. The transfer functions of the current PR controller and its HCs are represented by Han et al. (2017)

$$G_{TI}\ (s) = G^I_{PR}\ (s) + G^I_{HCs}\ (s) \tag{22}$$

$$G^I_{PR}\ (s) = K_{pI} + \frac{K_{rI}S}{S^2 + 2\omega_{cI}S + \omega_o^2} \tag{23}$$

$$G^I_{HCs}(s) = \sum_{h=5,7,11,13}^{n} \frac{K_{hI}S}{S^2 + 2\omega_{chI}S + (h\omega_o)^2} \tag{24}$$

The transfer functions of the voltage PR controller and its HCs can be expressed as (Han et al., 2017)

$$G_{TV}\ (s) = G^V_{PR}\ (s) + G^V_{HCs}\ (s) \tag{25}$$

$$G^V_{PR}\ (s) = K_{pV} + \frac{K_{rV}S}{S^2 + 2\omega_{cV}S + \omega_o^2} \tag{26}$$

$$G^V_{HCs}(s) = \sum_{h=5,7,11,13}^{n} \frac{K_{hV}S}{S^2 + 2\omega_{chV}S + (h\omega_o)^2} \tag{27}$$

The transfer function of the PWM delay is as follows

$$G_{PWM}\ (s) = \frac{1}{1 + 1.5T_{sa}s} \tag{28}$$

Here, $K_{pI}$, $K_{rI}$, $\omega_{cI}$, $K_{pV}$, and $\omega_{cV}$ are the proportional gain, resonant gain and cutoff frequency around the fundamental-frequency $\omega_o$ of PR current and voltage controller, respectively; $K_{hI}$, $\omega_{chI}$, $K_{hV}$ and $\omega_{chV}$ are the resonant gain and cutoff frequency around resonant-frequency $h\omega_o$ of current and voltage harmonic compensator for harmonic order $h$; $\omega_o$ is the fundamental frequency of microgrid; and $T_{sa}$ is the sampling time.

By using the model of the voltage closed-loop represented by (19)–(21), the bode plot diagrams of the voltage closed-loop in case of current/voltage PI controllers and also in case of current/voltage PR controllers with 5th, 7th, 11th and 13th harmonics tracking are depicted in Fig. 5. It can be observed that unlike PI controllers, the PR controllers with HCs provide a unity gain for voltage closed-loop response at the fundamental frequency and frequencies of 5th, 7th, 11th and 13th harmonics.

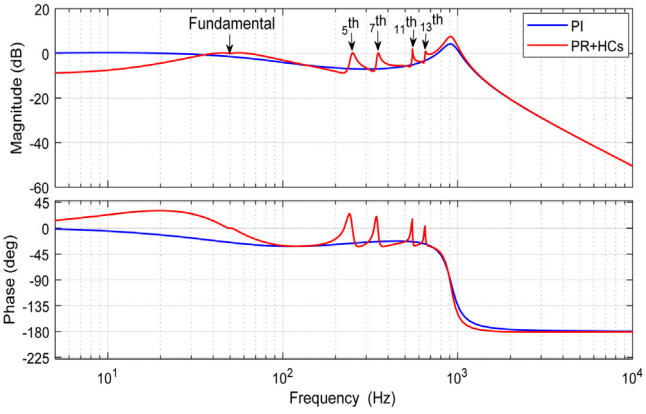


**Fig. 5.** Bode plot diagrams of the voltage closed-loop in case of current/voltage PI controllers and also in case of current/voltage PR controllers with 5th, 7th, 11th and 13th harmonics tracking.

Consequently, the system based on PR controllers and HCs has a superior performance in tracking capability without any steady-state error at both the fundamental frequency and frequencies of target harmonics.

### 3.2. Outer droop control loops

The droop control loops are responsible for realizing a proper active/reactive power-sharing among the paralleled grid-supporting VSIs-based DG units by using only low bandwidth communications. It is assumed that the grid-supporting VSIs-based DG units are integrated into the electrical power network via predominantly inductive distribution lines. Therefore, the active and reactive powers between the DG unit and the power network can be determined approximately as follows

$$P = \frac{V_{oi}V_{bus}}{X_{dl}} \varnothing \tag{29}$$

$$Q = \frac{V_{oi}}{X_{dl}} (V_{bus} - V_{oi}) \tag{30}$$

Here, $V_{oi}$ and $V_{bus}$ are the amplitude of the VSI output voltage and the amplitude of network bus voltage, respectively; $X_{dl}$ is the reactance of distribution line; and $\varnothing$ is the angle between $V_{bus}$ and $V_{oi}$ , which is called the load angle. Considering the network voltage has zero phase angle, the phase angle of inverter voltage will be equal to $\varnothing$. Consequently, the droop control strategy can be employed to control and adjust the amplitude and phase angle of the voltage reference signal according to the reactive and active power, respectively, guaranteeing reactive and active flow control. According to this, the droop control characteristics can be defined as follows:

$$\varnothing^* = \varnothing_r - \frac{K_{pDP}S + K_{iDP}}{S}(P - P^*) \tag{31}$$

$$V^* = V_r - K_{pDQ}(Q - Q^*) \tag{32}$$

Here, $V^*$ and $\varnothing^*$ are the references of the voltage amplitude and its phase angle, respectively; $V_r$ and $\varnothing_r$ are the nominal values of the voltage amplitude and phase angle, respectively; $K_{pDP}$ and $K_{iDP}$ are the proportional and integral droop coefficients for active power control, respectively; $K_{pDQ}$ is the proportional droop coefficient for reactive power control; and $P$, $Q$, $P^*$ and $Q^*$ are the active and reactive powers, and their references, respectively. The $P^*$ and $Q^*$ must be adjusted to zero in the islanded operation. The active and reactive powers can be calculated in stationary $\alpha\beta$-frame as follow (Vasquez et al., 2013)

$$\begin{cases} P = \dfrac{\omega_{cL}}{S + \omega_{cL}} \left(V_{c\alpha} i_{o\alpha} + V_{c\beta} i_{o\beta}\right) \\ Q = \dfrac{\omega_{cL}}{S + \omega_{cL}} \left(V_{c\beta} i_{o\alpha} + V_{c\alpha} i_{o\beta}\right) \end{cases} \tag{33}$$

Here, $V_{c\alpha}$, $V_{c\beta}$, $i_{o\alpha}$ and $i_{o\beta}$ are the voltage across filter capacitor and the inverter output current in $\alpha$- and $\beta$-axis, respectively; and $\omega_{cL}$ is the cutoff frequency of the low pass filter, which is used to eliminate the ripples in active and reactive powers.

### 3.3. Intermediate virtual impedance loops

The virtual impedance loops are employed to make the inverter output impedance more inductive for decreasing the cross-coupling between active and reactive power, improving the VSIs stability, reducing the circulating currents and damping the active/reactive power oscillations. The stability of the droop control approach is enhanced by adding the virtual impedance without causing power losses and additional cost. The loops of virtual impedance can be represented in $\alpha\beta$-frame as follow (Vasquez et al., 2013)

$$\begin{cases} V_{vir\alpha} = R_{vir} i_{o\alpha} - \omega_o L_{vir} i_{o\beta} \\ V_{vir\beta} = R_{vir} i_{o\beta} - \omega_o L_{vir} i_{o\alpha} \end{cases} \tag{34}$$

Here, $R_{vir}$ and $L_{vir}$ are the resistance and inductance of the virtual impedance, respectively; and $V_{vir\alpha}$ and $V_{vir\beta}$ are the voltage correction signal of the virtual impedance loop in $\alpha$-and $\beta$-axis, respectively.

## 4. Secondary and synchronization controls of grid-supporting VSIs

The droop control characteristics lead the microgrid's frequency and voltage amplitude to deviate from their nominal values. Consequently, the SCL is necessary to eliminate these voltage/frequency deviations for restoring their reference values. The frequency deviation should be corrected by the SCL to be within the permissible limits recommended by the grid exigencies in Technical Paper (2008). The block diagram of the SCL is demonstrated in Fig. 6. To generate the restoration signals of secondary control to nullify the voltage/frequency deviations created by droop loops, the amplitude and angular frequency of the microgrid voltage, $\omega_{MG}^{meas}$ and $E_{MG}^{meas}$, are sensed and compared with their references $\omega_{MG}^{*}$ and $E_{MG}^{*}$. Afterward, the different errors are remedied throughout PI controllers to produce the correction signals of SCL to be sent to the control loops of the droop approach for each grid-supporting VSI. The SCL compensation signals $\delta\omega_{\text{sec}}^{comp}$ and $\delta E_{\text{sec}}^{comp}$ can be expressed as (Vasquez et al., 2013)

$$\delta\omega_{\text{sec}}^{comp} = K_{psf}(\omega_{MG}^{*} - \omega_{MG}^{meas}) + K_{isf} \int \left(\omega_{MG}^{*} - \omega_{MG}^{meas}\right) dt + \Delta\theta_{syn} \tag{35}$$

$$\delta E_{\text{sec}}^{comp} = K_{psE}(E_{MG}^{*} - E_{MG}^{meas}) + K_{isE} \int \left(E_{MG}^{*} - E_{MG}^{meas}\right) dt + \Delta E_{syn} \tag{36}$$

Here, $K_{psf}$, $K_{isf}$, $K_{psE}$ and $K_{isE}$ are the proportional and integral gains of frequency and voltage amplitude secondary PI controllers, respectively; $\omega_{MG}^{*}$, $\omega_{MG}^{meas}$, $E_{MG}^{*}$ and $E_{MG}^{meas}$ are the reference and measured values of angular frequency and voltage amplitude, respectively; and $\Delta\theta_{syn}$ and $\Delta E_{syn}$ are the compensation signals of synchronization control level which are zero when the external power grid is not present.

In order to prepare the microgrid to be connected to the external power grid, the microgrid's frequency, and voltage amplitude and phase should be synchronized with those of the external main grid to ensure a seamless transition. Before reconnecting back the microgrid to the external power grid, the error differences in frequency, and voltage amplitude and phase between them must be met by the recommendations of DG units' synchronization by IEEE Standard 1547–2003. The block diagram of the synchronization control level is displayed in Fig. 6. The synchronization signals, $\Delta\theta_{syn}$ and $\Delta E_{syn}$, should be fed to the control loops of droop approach to compensate the error differences in frequency, and voltage amplitude and phase can be expressed as (Sun et al., 2017)

$$\Delta\theta_{syn} = \left(K_{p\theta}^{syn} + K_{i\theta}^{syn}/S\right)\left(-v_{EG\alpha} v_{MG\beta} + v_{EG\beta} v_{MG\alpha}\right) \tag{37}$$

$$\Delta E_{syn} = \left(K_{pE}^{syn} + K_{iE}^{syn}/S\right)\left(\sqrt{v_{EG\alpha}^2 + v_{EG\beta}^2} - \sqrt{v_{MG\alpha}^2 + v_{MG\beta}^2}\right) \tag{38}$$

Here, $K_{p\theta}^{syn}$, $K_{i\theta}^{syn}$, $K_{pE}^{syn}$ and $K_{iE}^{syn}$ are the proportional and integral gains of frequency and voltage amplitude PI synchronization compensators, respectively; and $v_{MG\alpha}$, $v_{MG\beta}$, $v_{EG\alpha}$ and $v_{EG\beta}$ are the microgrid and external grid voltages in $\alpha$- and $\beta$-axis, respectively.

## 5. Optimal design procedures of microgrid's controllers and HCs

The proposed optimal design procedures of microgrid controllers and HCs are employed to achieve the study objectives mentioned above. These procedures are based on a new H-HHOPSO algorithm that cooperated with proposed multi-objective functions. In this paper, the design procedures are carried out through two stages. In the first stage, the parameters of current/voltage PR controllers with their additional HCs for the PCL are optimally designed. However, the second stage is used to design the controllers' coefficients of droop control, SCL and synchronization control level.

### 5.1. First stage optimization procedure

The first stage is employed to tackle the design problem of twenty-two parameters of current/voltage PR controllers with their HCs for the PCL. The proposed multi-objective error function, mentioned in (39), was selected to reduce the THD in the microgrid voltage, and also to minimize the arithmetic summation of the following: the integral time absolute error (ITAE) of $\alpha$-axis voltage, ITAE of $\beta$-axis voltage, $\alpha$-axis current and ITAE of $\beta$-axis current. The optimization problem for optimal designing the parameters of current/voltage PR controllers with their HCs, which is proposed by the authors, can be formulated as Consider $\vec{x}$ which is given in Box I

$$\text{Minimize } FF = \alpha_1 THD_V + \alpha_2 \left(\int_0^\infty t.|e_{V\alpha}|\,dt + \int_0^\infty t.|e_{V\beta}|\,dt + \int_0^\infty t.|e_{I\alpha}|\,dt + \int_0^\infty t.|e_{I\beta}|\,dt\right)$$

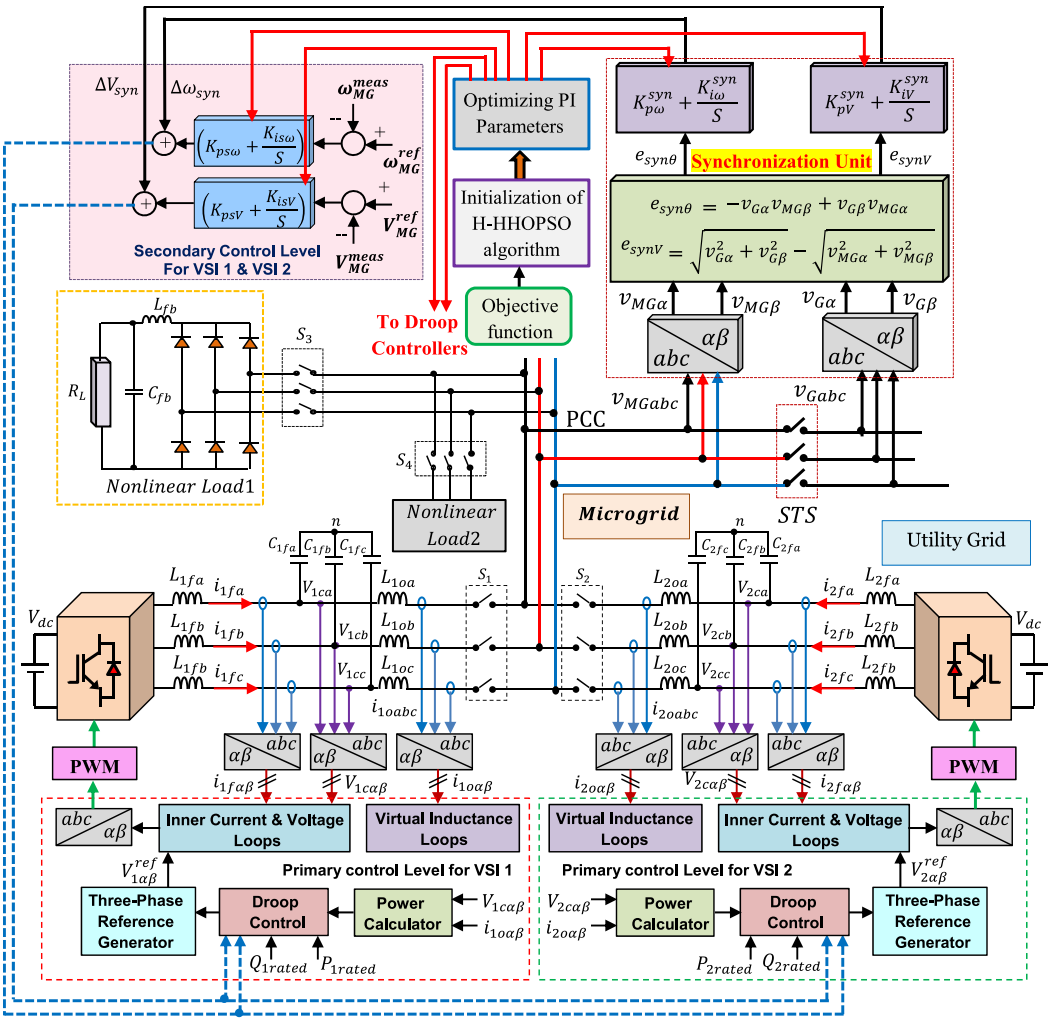


**Fig. 6.** Block diagram of the whole microgrid system including two grid-supporting VSIs based on the proposed control approach developed in $\alpha\beta$-frame and depended on the optimal controllers and HCs.

$$\text{Consider } \overrightarrow{x} = \begin{bmatrix} \overrightarrow{X_V} \\ \overrightarrow{X_I} \end{bmatrix} = \begin{bmatrix} K_{pV} & K_{rV} & K_{5V} & K_{7V} & K_{11V} & K_{13V} & \omega_{cV} & \omega_{c5V} & \omega_{c7V} & \omega_{c11V} & \omega_{c13V} \\ K_{pI} & K_{rI} & K_{5I} & K_{7I} & K_{11I} & K_{13I} & \omega_{cI} & \omega_{c5I} & \omega_{c7I} & \omega_{c11I} & \omega_{c13I} \end{bmatrix}$$

**Box I.**

$$\text{Variable range} \begin{cases} 0.05 \le K_{pV} \le 5 \\ 100 \le K_{rV} \le 1000 \\ 2 \le K_{hV} \le 100 \\ 2 \le K_{pI} \le 20 \\ 20 \le K_{rI} \le 200 \\ 1 \le K_{hI} \le 100 \\ 1 \le 2\omega_{cV} \le 10 \\ 5 \le 2\omega_{chV} \le 250 \\ 1 \le 2\omega_{cI} \le 5 \\ 20 \le 2\omega_{chI} \le 250 \end{cases} \quad (39)$$

Here, $e_{V\alpha}$, $e_{V\beta}$, $e_{I\alpha}$ and $e_{I\beta}$ are the errors of the voltage and current in $\alpha$- and $\beta$-axis, respectively; $THD_V$ is the THD in the microgrid voltage, and $\propto_1$ and $\propto_2$ are the priority weights for terms in the above multi-objective function. Fig. 7 depicts a flowchart of the first stage of the proposed design guidelines for obtaining the optimal parameters of current/voltage PR controllers with HCs. Initially, the fitness function (FF) is calculated during the run of the simulation model. The FF will be fed as input to the H-HHOPSO algorithm with other inputs, including search agents' number, upper/lower limits of variables, maximum iterations number and search agent's dimension. The H-HHOPSO algorithm will generate an initial random vector of controllers' parameters for each search agent, which represents a possible solution in search space. Then, the initial vector will be updated throughout the strategy of H-HHOPSO algorithm. Finally, the obtained results of H-HHOPSO algorithm are evaluated and compared with those of other meta-heuristic optimization algorithms, including grey wolf optimizer (GWO) (Mirjalili et al., 2014), particle swarm optimization (PSO) and HHO, to get the finest parameters. In this optimization problem, each

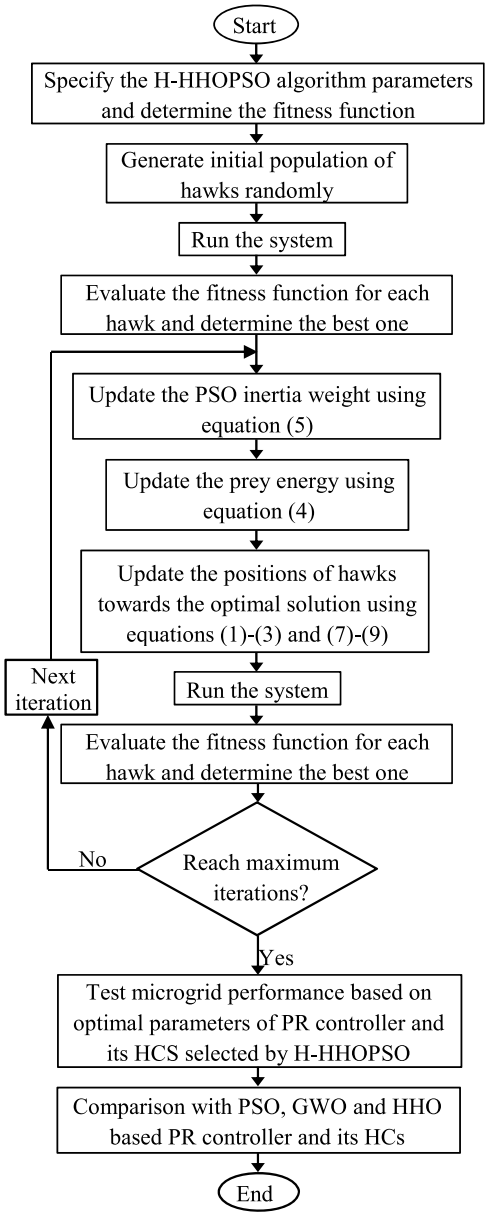


**Fig. 7.** A flowchart of the first stage of the proposed design guidelines for obtaining the optimal parameters of current/voltage PR controllers with HCs.

Harris hawk represents a search agent exploited to search and find the best parameters of current/voltage PR controllers and their HCs. In this paper, the initial parameters of algorithms are selected as following: maximum iteration number = 30, search agents number = 20, search dimension in first stage = 22, search dimension in second stage = 11 and number of runs for each algorithm = 10. Fig. 8 shows the convergence curves of the PSO, GWO, HHO and H-HHOPSO algorithms for minimizing the multi-objective function illustrated in (39). The optimization objective was to minimize the multi-objective function, and therefore its lowest value has been considered as the best value. It can be observed from Fig. 8 that the minimum obtained values of multi-objective are 3.922133, 2.978833, 2.36785 and 1.231183 in the cases of PSO, GWO, HHO and H-HHOPSO algorithm, respectively. Consequently, the H-HHOPSO algorithm gives a better optimum solution than the other algorithms.

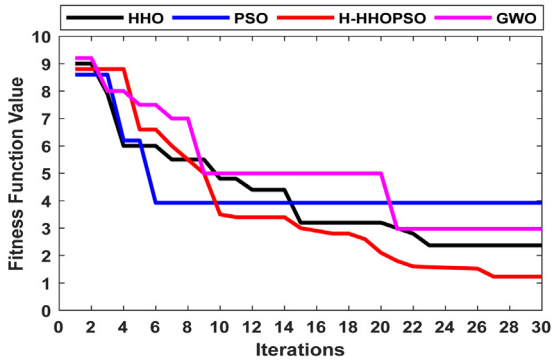


**Fig. 8.** Convergence curves of the PSO, GWO, HHO and H-HHOPSO algorithms for minimizing the multi-objective function illustrated in (39).

### 5.2. Second stage optimization procedure

After the first stage is performed, the second stage is conducted in this subsection. The second stage is used to optimally tune eleven controllers' parameters for both the SCL and synchronization control levels. The suggested objective function, mentioned in (40), was designated to minimize the arithmetic summation of the following: ITAE in both real and reactive powers of droop control, ITAE in both frequency and voltage amplitude of SCL, and ITAE in both phase angle and voltage amplitude of synchronization control level. In this stage, the formulation of the optimization problem can be proposed as follows

Consider

$$\left[K_{pDP} \quad K_{iDP} \quad K_{pDQ} \quad K_{psf} \quad K_{isf} \quad K_{psE} \quad K_{isE} \quad K_{p\theta}^{syn} \quad K_{i\theta}^{syn} \quad K_{pE}^{syn} \quad K_{iE}^{syn}\right]$$

$$\text{Minimize } FF = \int_0^\infty t.\left|e_P\right| dt + \int_0^\infty t.\left|e_Q\right| dt + \int_0^\infty t.\left|e_{secf}\right| dt + \int_0^\infty t.\left|e_{secE}\right| dt + \int_0^\infty t.\left|e_{syn\theta}\right| dt + \int_0^\infty t.\left|e_{synE}\right| dt$$

$$\text{Variable range} \begin{cases} 1e-6 \le K_{pDP} \le 1e-4 \\ 0.0001 \le K_{iDP} \le 0.001 \\ 0.0005 \le K_{pDQ} \le 0.01 \\ 0.001 \le K_{psf} \le 0.1 \\ 0.01 \le K_{isf} \le 15 \\ 0.01 \le K_{psE} \le 1 \\ 0.1 \le K_{isE} \le 100 \\ 0.001 \le K_{p\theta}^{syn} \le 0.1 \\ 0.0001 \le K_{i\theta}^{syn} \le 0.01 \\ 0.01 \le K_{pE}^{syn} \le 0.2 \\ 0.0001 \le K_{iE}^{syn} \le 0.03 \end{cases} \tag{40}$$

Here, $e_P$ and $e_Q$ are the errors in active and reactive powers of droop control, respectively; $e_{secf}$ and $e_{secE}$ are the errors in frequency and voltage amplitude of SCL, respectively; and $e_{syn\theta}$ and $e_{synE}$ are the errors in phase angle and voltage amplitude of synchronization control level, respectively.

## 6. Simulation results and discussions

The feasibility of two-stage optimal design procedures is examined throughout the two scenarios. The first scenario evaluates the efficiency of the first design stage for the inner current and voltage feedback loops which depend on PR controllers with their HCs. After the first stage is investigated, the whole microgrid system is tested and evaluated in the second scenario. This whole

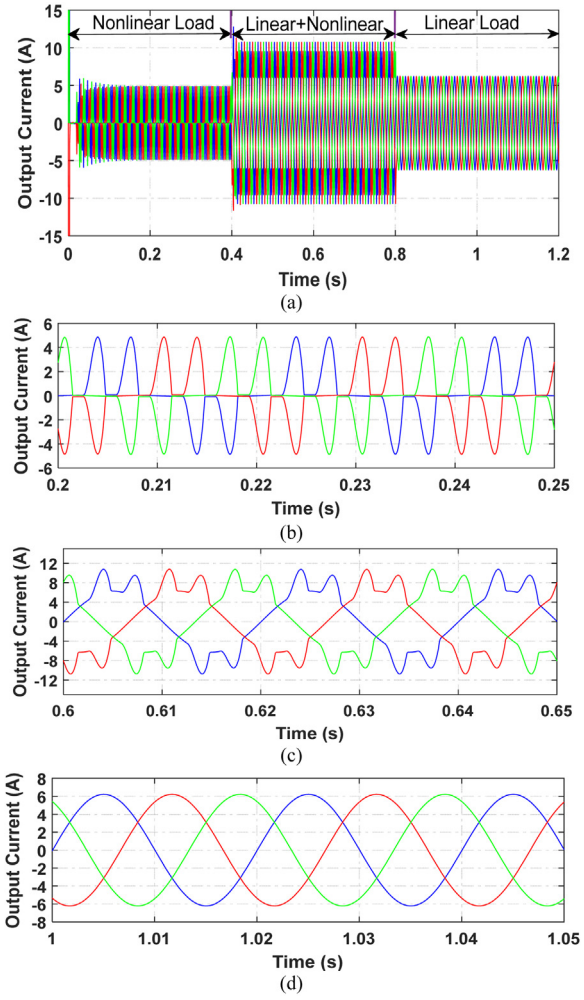


**Fig. 9.** Three-phase output currents during linear, nonlinear and composite loads in the case of the proposed voltage and current PR controllers plus their HCs (a) Three-phase output currents; (b) zoomed-in view for nonlinear load currents; (c) zoomed-in view for linear plus nonlinear load currents; (d) Zoomed-in view for linear load currents.

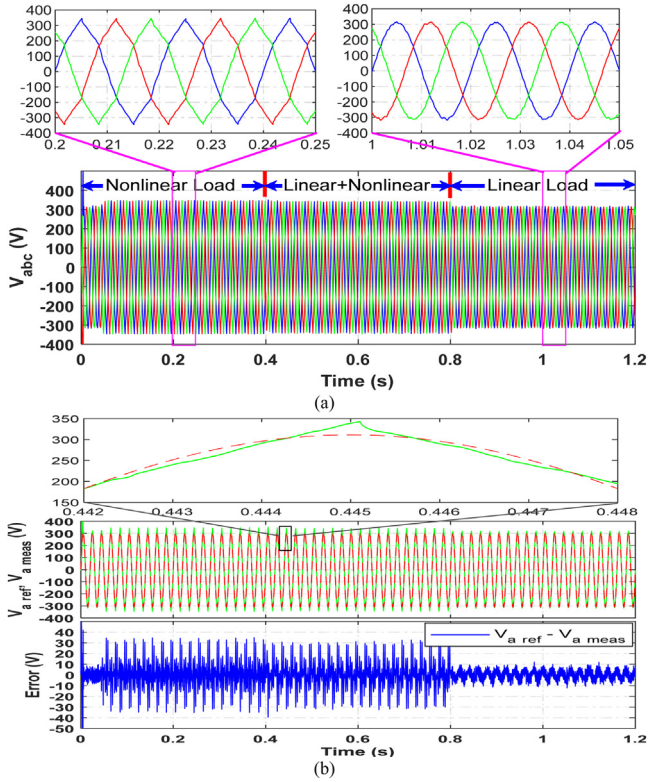


**Fig. 10.** Output voltages during linear, nonlinear and composite loads in the case of the proposed voltage and current PI conventional controllers (a) three-phase output voltages; (b) phase-a actual voltage and its reference with the error between them.

system has three control levels based on the controllers and HCs designed by the proposed optimal procedures conducted through two stages.

### 6.1. Scenario I

In this scenario, it is necessary to evaluate the first stage effectiveness of design procedures for voltage/current PR controllers with their HCs. Consequently, a microgrid comprising of one DG unit, based on only the primary control approach, shown in Fig. 3, is modeled and simulated through a MATLAB environment. In this case, the control system consists of only inner feedback control loops of voltage and current, in which the three-phase voltage references are generated internally not from droop control loops. The optimal voltage/current PR controllers with their HCs, based on H-HHOPSO algorithm, are examined under the linear load of 50 Ω, nonlinear load comprising diode bridge rectifier connected to 300 Ω resistive load and both the two loads (i.e. linear + nonlinear). The performance is evaluated and compared with the conventional PI controllers, PR controllers without HCs, and PSO, HHO and GWO-based PR controllers with HCs. Fig. 9 depicts the three-phase output currents during linear, nonlinear and linear + nonlinear (composite) loads in the case of the proposed voltage/current PR controllers plus their HCs. Figs. 10–12 illustrate the three-phase output voltages as well as phase-a actual voltage and its reference with the error between them during linear, nonlinear and composite loads in cases of conventional PI controllers, PR controllers without HCs and proposed optimal PR controllers with their HCs, respectively. It can be observed that the proposed optimal PR controller with their HCs has a superior performance in tracking the sinusoidal reference voltage with only slight oscillations. However, the PR controllers without HCs suffer from significant fluctuations in sinusoidal output voltage, which are increased in the case of conventional PI controllers. Figs. 13–15 demonstrate the harmonics spectrum of the output voltage during linear, nonlinear and composite loads in the cases of conventional PI controllers, PR controllers without HCs and proposed optimal PR controllers with their HCs, respectively. It can be observed that the THD in the output voltage during nonlinear load decreased from 5.23% in the case of conventional PI controllers to 4.18% in the case of PR controllers without HCs to 0.16% in the case of optimal PR controllers with their HCs. Table 1 gives the individual harmonics amplitudes and THD of output microgrid voltage during linear, nonlinear and composite loads in the cases of current/voltage PI controllers, PR controllers without HCs and optimal PR controllers plus their HCs. It can be observed that unlike the PI controllers and PR controllers without HCs, the optimal PR controllers with their HCs have the minimum values of both individual harmonics amplitudes and THD in the output voltage during linear, nonlinear and composite loads. Fig. 16 shows a comparative graph of individual harmonic magnitudes between

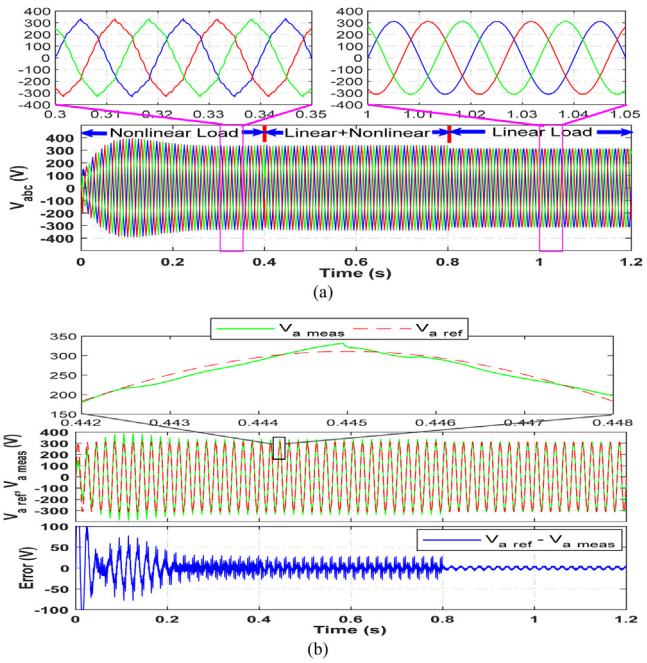


**Fig. 11.** Output voltages during linear, nonlinear and composite loads in the case of the proposed voltage and current PR controllers without HCs (a) three-phase output voltages; (b) phase-a actual voltage and its reference with the error between them.

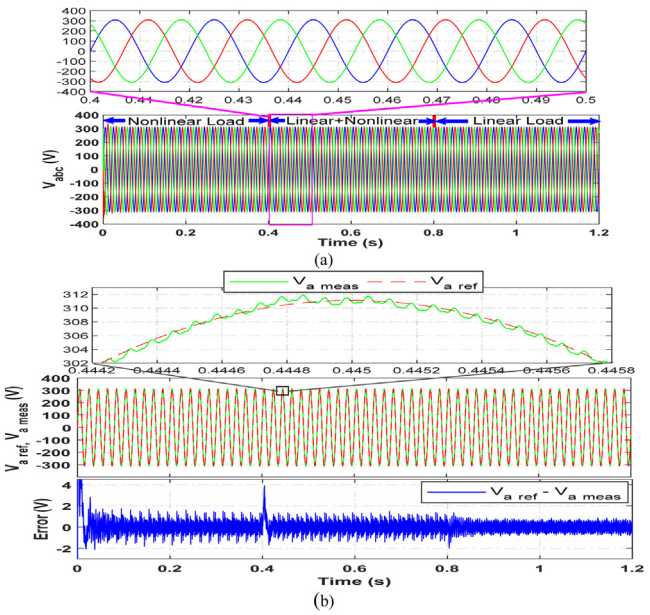


**Fig. 12.** Output voltages during linear, nonlinear and composite loads in the case of the proposed voltage and current PR controllers plus their HCs (a) three-phase output voltages; (b) phase-a actual voltage and its reference with the error between them.

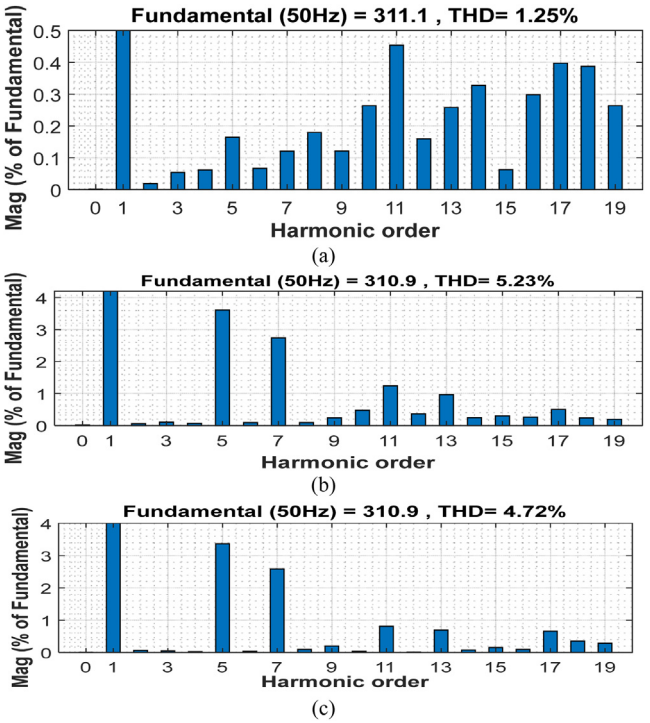


**Fig. 13.** Harmonics spectrum of the output voltage during linear, nonlinear and composite loads in the case of the voltage and current PI conventional controllers (a) linear load; (b) nonlinear load; (c) composite load.

the proposed optimal PR controller plus its HCs, PR controllers without HCs, and conventional PI controller under different types of load. Fig. 17 demonstrates the six switching pulses for grid-supporting inverter in the case of H-HHOPSO algorithm. Table 2 represents the optimal parameters obtained by the proposed design guidelines for PR voltage/current PR controllers with their HCs. The only limitation of the work presented in this paper is that the parameters obtained from the proposed guidelines may only need to fine-tune in practical and realistic operating condition. It can be observed from Table 2 that the computational times for H-HHOPSO, HHO, GWO and PSO algorithms are 159.213 min, 167.845 min, 182.357 min and 162.638 min, respectively. The proposed H-HHOPSO algorithm has a lower computational time than the other studied algorithms. The studied algorithms were run through a computer with installed memory (RAM) of 8.0 GB and processor of Intel(R) Core(TM) i7-4510U CPU@ 2.0 GHz. The computational times for the studied algorithms in this paper can be extremely reduced by using high performance computing facility. Fig. 18 clarifies the harmonics spectrum of the output voltage during nonlinear load in the cases of PSO, GWO and HHO-based voltage/current PR controllers with their HCs. It can be observed that the THD in the output voltage during nonlinear load decreased from 3.28% to 2.81% to 1.75% in cases of PSO, GWO and HHO-based voltage/current PR controllers with their HCs, respectively. Table 3 presents the individual harmonics amplitudes and THD of output microgrid voltage during linear, nonlinear and composite loads in the cases of H-HHOPSO, HHO, GWO and PSO-based voltage/current PR controllers with their HCs. At any operating conditions, the proposed optimal PR controllers with their HCs meet the exigencies recommended by IEEE/IEC harmonics standards and also have the best performance in minimizing both individual harmonic amplitudes and THD of the microgrid's output voltage.

### 6.2. Scenario II

In this scenario, the whole microgrid system, based on three control levels that cooperated with the optimal controllers and HCs designed by the proposed guidelines, is examined. In order to test the effectiveness of the proposed control methodology based on the optimal controllers and HCs, a microgrid consisting of two identical grid-supporting VSIs was modeled in stationary $\alpha\beta$-frame and simulated in MATLAB environment. The microgrid under test, including the three control levels, is shown in Fig. 6 with the power circuit parameters and the optimal coefficients of the controllers and HCs listed in Tables 2 and 4.

**Table 1**
The individual harmonics amplitudes and THD of output microgrid voltage during linear, nonlinear and composite loads in the cases of current/voltage PI controllers, PR controllers without HCs and optimal PR controllers plus their HCs.

| Fundamental/ Harmonic order/ THD | Controller type | | | | | | | | |
|---|---|---|---|---|---|---|---|---|---|
| | PI controller | | | PR controller without HCs | | | Proposed PR controller Plus HCs | | |
| | Nonlinear | Linear | Linear + Nonlinear | Nonlinear | Linear | Linear + Nonlinear | Nonlinear | Linear | Linear + Nonlinear |
| Fundamental | 310.9 V (peak) (100%) | 311.1 V (peak) (100%) | 310.9 V (peak) (100%) | 311 V (peak) (100%) | 311 V (peak) (100%) | 311.2 V (peak) (100%) | 311.1 V (peak) (100%) | 311 V (peak) (100%) | 311 V (peak) (100%) |
| 3rd | 0.1044% | 0.05365% | 0.04772% | 0.08611% | 0.03597% | 0.03493% | 0.001025% | 0.001471% | 0.002291% |
| 5th | 3.609% | 0.1647% | 3.369% | 2.273% | 0.04128% | 2.215% | 0.03411% | 0.00438% | 0.02893% |
| 7th | 2.739% | 0.1205% | 2.588% | 2.224% | 0.01596% | 2.29% | 0.03667% | 0.000956% | 0.03492% |
| 9th | 0.2413% | 0.121% | 0.1989% | 0.08025% | 0.02327% | 0.04919% | 0.00199% | 0.002389% | 0.005536% |
| 11th | 1.239% | 0.4539% | 0.809% | 1.049% | 0.05646% | 1.005% | 0.06105% | 0.006113% | 0.05723% |
| 13th | 0.9645% | 0.2584% | 0.6902% | 0.8718% | 0.06237% | 0.698% | 0.03738% | 0.000959% | 0.03775% |
| 15th | 0.3004% | 0.06279% | 0.1516% | 0.1841% | 0.04342% | 0.0365% | 0.0001332% | 0.000428% | 0.001305% |
| 17th | 0.5013% | 0.3973% | 0.6586% | 1.912% | 0.1461% | 1.072% | 0.02925% | 0.002429% | 0.02984% |
| 19th | 0.1941% | 0.2639% | 0.2853% | 1.122% | 0.13% | 0.3699% | 0.02938% | 0.001787% | 0.02923% |
| THD | 5.23% | 1.25% | 4.72% | 4.18% | 0.63% | 3.64% | 0.16% | 0.12% | 0.16% |

**Table 2**
The optimal parameters were obtained by the proposed design guidelines for PR voltage and current PR controllers with their HCs.

| Parameters of PR controllers and their HCs | H-HHOPSO | HHO | PSO | GWO |
|---|---|---|---|---|
| $K_{pV}$ | 1.833792 | 3.370431 | 0.10303 | 1.328514 |
| $K_{rV}$ | 796.9437 | 764.6223 | 672.7865 | 346.5463 |
| $K_{5V}$ | 80.62862 | 18.38088 | 80.47264 | 57.14535 |
| $K_{7V}$ | 94.61034 | 27.30676 | 40.03947 | 77.5617 |
| $K_{11V}$ | 17.7901 | 27.01649 | 27.01085 | 23.63293 |
| $K_{13V}$ | 91.04992 | 4.28428 | 29.09901 | 50.16397 |
| $2\omega_{cV}$ | 5.02142 | 1.870677 | 8.856286 | 4.112025 |
| $2\omega_{c5V}$ | 5.274829 | 85.3602 | 99.27128 | 55.75242 |
| $2\omega_{c7V}$ | 104.6628 | 129.9165 | 141.9648 | 49.75813 |
| $2\omega_{c11V}$ | 160.7646 | 10.75371 | 95.93607 | 51.4355 |
| $2\omega_{c13V}$ | 117.5536 | 239.1812 | 31.68606 | 216.4337 |
| $K_{pI}$ | 17.84921 | 7.767538 | 14.30152 | 4.344418 |
| $K_{rI}$ | 148.7882 | 27.79968 | 58.97532 | 195.2092 |
| $K_{5I}$ | 45.67919 | 35.45971 | 58.42796 | 30.38284 |
| $K_{7I}$ | 1.065081 | 51.02254 | 25.49977 | 68.90601 |
| $K_{11I}$ | 5.719752 | 53.75801 | 93.65477 | 37.71907 |
| $K_{13I}$ | 22.12468 | 40.88535 | 56.89113 | 39.22372 |
| $2\omega_{cI}$ | 4.280542 | 3.985016 | 1.109482 | 1.221704 |
| $2\omega_{c5I}$ | 59.82435 | 99.92674 | 38.97316 | 86.59314 |
| $2\omega_{c7I}$ | 91.6601 | 81.81544 | 83.95773 | 125.5591 |
| $2\omega_{c11I}$ | 28.68581 | 161.1439 | 184.5246 | 93.71798 |
| $2\omega_{c13I}$ | 192.0994 | 196.4462 | 233.61 | 192.9981 |
| FF value at nonlinear load | 1.231183 | 2.36785 | 3.922133 | 2.978833 |
| $THD_v$ at nonlinear load | 0.16% | 1.75% | 3.28% | 2.81% |
| $THD_v$ at computed parameters+10% | 0.18% | 1.87% | 3.58% | 2.97% |
| $THD_v$ at computed parameters−10% | 0.21% | 1.95% | 3.74% | 3.26% |
| Computational cost (Min) | 159.213 | 167.845 | 182.357 | 162.638 |

The system parameters, listed in Table 4, were taken as the following: the parameters of power circuit were taken from the literature (Vasquez et al., 2013). However, the control parameters were selected by the optimal design procedures discussed in this paper. The performance of the proposed model is tested under ±10% variations around the computed parameters listed in Table 2. When the values of the controllers' parameters are varied in the range of ±10%, the THD in microgrid's voltage is slightly affected. The tested microgrid is loaded by two nonlinear loads, each represented by a three-phase diode bridge rectifier connected to a resistive load of 8 ohm through an LC filter. The performance of the microgrid is examined under the nonlinear load change, and also during the suddenly disconnecting of one grid-supporting inverter. Moreover, the compensation of deviations in phase angle, frequency and voltage amplitude, by using SCL and synchronization control level, is verified and confirmed in this section. Fig. 19 describes the microgrid voltage during nonlinear loads in case of using the optimal current/voltage PR controllers with HCs. When the HCs are deactivated, the voltage THD is 5.82% decreased to 0.19% by activating voltage/current PR controllers with HCs. Table 5 presents a comparative study between our proposed optimal PR controllers with their HCs and the previously introduced controllers in the literatures. It can be observed that the proposed optimal procedures in this paper have better results than the previously published researches in this scope. Fig. 20 depicts the waveforms of output currents for the two paralleled grid-supporting inverters sharing the two nonlinear loads via the droop control methodology.

It is worth mentioning that Figs. 21 and 22 demonstrate the transient response of the microgrid's frequency and voltage, respectively, with and without secondary control under the nonlinear load change at t = 0.5 s and during the suddenly disconnecting of one inverter at t = 1 s. At any operating conditions, it can be observed that the deviations in microgrid's voltage amplitude

**Table 3**
The individual harmonics amplitudes and THD of output microgrid voltage during linear, nonlinear and composite loads in the cases of H-HHOPSO, HHO, GWO and PSO-based voltage and current PR controllers with their HCs.

| Fundamental/ Harmonic order/ THD | Controller type | | | | | | | | | | | |
|---|---|---|---|---|---|---|---|---|---|---|---|---|
| | H-HHOPSO based PR+HCs | | | HHO based PR+HCs | | | GWO based PR+HCs | | | PSO based PR+HCs | | |
| | Nonlinear | Linear | Linear + Nonlinear | Nonlinear | Linear | Linear + Nonlinear | Nonlinear | Linear | Linear + Nonlinear | Nonlinear | Linear | Linear + Nonlinear |
| Fundamental | 311.1V (peak) (100%) | 311V (peak) (100%) | 311V (peak) (100%) | 311.3 V (peak) (100%) | 311.1 V (peak) (100%) | 311 V (peak) (100%) | 311.1 V (peak) (100%) | 311.1 V (peak) (100%) | 310.9 V (peak) (100%) | 311 V (peak) (100%) | 311 V (peak) (100%) | 310.9 V (peak) (100%) |
| 3rd | 0.00103% | 0.001471% | 0.00229% | 0.04547% | 0.014% | 0.0179% | 0.0661% | 0.0416% | 0.01% | 0.0353% | 0.0443% | 0.0244% |
| 5th | 0.0341% | 0.00438% | 0.02893% | 0.1896% | 0.025% | 0.1173% | 0.2629% | 0.0777% | 0.2118% | 0.4879% | 0.1385% | 0.4627% |
| 7th | 0.03667% | 0.000956% | 0.03492% | 0.1442% | 0.0426% | 0.1535% | 0.1537% | 0.1297% | 0.1354% | 0.5232% | 0.1583% | 0.645% |
| 9th | 0.00199% | 0.002389% | 0.00554% | 0.05449% | 0.001% | 0.0622% | 0.0852% | 0.0186% | 0.052% | 0.0516% | 0.1788% | 0.1308% |
| 11th | 0.06105% | 0.006113% | 0.05723% | 0.08558% | 0.0477% | 0.0493% | 0.1999% | 0.0447% | 0.1207% | 0.4692% | 0.0908% | 0.4014% |
| 13th | 0.03738% | 0.000959% | 0.03775% | 0.03992% | 0.0262% | 0.0456% | 0.1556% | 0.0828% | 0.1162% | 0.1958% | 0.0542% | 0.116% |
| 15th | 0.00013% | 0.000428% | 0.0013% | 0.02133% | 0.0149% | 0.0371% | 0.0805% | 0.0679% | 0.0558% | 0.2747% | 0.121% | 0.2299% |
| 17th | 0.02925% | 0.00243% | 0.02984% | 0.01926% | 0.0295% | 0.0366% | 0.116% | 0.0589% | 0.0852% | 0.4589% | 0.1849% | 0.5% |
| 19th | 0.02938% | 0.00178% | 0.02923% | 0.04736% | 0.0458% | 0.0643% | 0.0894% | 0.0602% | 0.0523% | 0.4767% | 0.1275% | 0.1767% |
| THD | 0.16% | 0.12% | 0.16% | 1.75% | 1.18% | 1.59% | 2.81% | 1.42% | 2.3% | 3.28% | 1.74% | 2.76% |

**Table 4**
The parameters of the microgrid under study and its optimal controllers' coefficients.

| Parameter | Symbol | Value |
|---|---|---|
| Power stage | | |
| Nominal microgrid voltage | $V$ | 311.13 V |
| Nominal microgrid frequency | $f$ | 50 Hz |
| DC-bus voltage | $V_{dc}$ | 750 V |
| Capacitance of filter | $C_f$ | 25 μF |
| Inductance of filter | $L_f$ | 1.8 mH |
| Inductance of output | $L_o$ | 1.8 mH |
| Linear resistive load | $R_L$ | 50 Ω |
| Nonlinear linear load | $L_{fb}$, $C_{fb}$, $R_L$ | 84 μH, 235 μF, 8/300 Ω |
| Switching frequency | $f_{sw}$ | 15 kHz |
| Droop Control | | |
| Proportional droop coefficient of frequency | $K_{pDP}$ | 6.57e−5 rad/W s |
| Integral droop coefficient of frequency | $K_{iDP}$ | 0.0008396 rad/W |
| Proportional droop coefficient of voltage amplitude | $K_{pDQ}$ | 0.001288 V/VAR |
| Resistance of virtual impedance | $R_{vir}$ | 0.8 Ω |
| Inductance of virtual impedance | $L_{vir}$ | 3.6 mH |
| Secondary control level | | |
| Proportional and integral terms of frequency secondary controller | $K_{psf}$ | 0.065 |
| | $K_{isf}$ | 6.84 |
| Proportional and integral terms of voltage secondary controller | $K_{psE}$ | 0.573 |
| | $K_{isE}$ | 80.42 |
| Synchronization control level | | |
| Proportional and integral terms of frequency synchronization controller | $K_{p\theta}^{syn}$ | 0.036 |
| | $K_{i\theta}^{syn}$ | 0.00038 |
| Proportional and integral terms of frequency synchronization controller | $K_{pE}^{syn}$ | 0.016 |
| | $K_{iE}^{syn}$ | 0.00086 |

and frequency, generated by the control loops of droop approach and virtual impedance, are successfully nullified utilizing the SCL strategy. The microgrid's voltage amplitude and frequency are recovered smoothly with a faster response than those clarified in Technical Paper (2008) required by the grid. Furthermore, Fig. 23 displays the achievement of the synchronization procedure between the external main grid and the microgrid. It can be observed that the instantaneous voltage waveforms of the external power grid and the microgrid are synchronized, and the difference (error) between them is decreased rapidly. This result highlights the high performance of the synchronization control level for realizing the seamless transitions during connecting/disconnecting to/from the external main power grid. The synchronization process is accomplished considering the synchronization requirements of DG units presented in IEEE standard (2014) demanded by IEEE Std. 1547–2014.

Finally, the active/reactive power-sharing between the two grid-supporting VSIs is illustrated in Fig. 24. From the initiation to t = 0.5 s, the two grid-supporting inverters are connected to the isolated microgrid and supplied the two local nonlinear loads. The power and current demanded by these loads are shared equally between two inverters. After t = 0.5 s, one load is suddenly disconnected; therefore the output active/reactive power and current for each inverter are decreased with equally sharing to only compensate the active/reactive power and current required by one load. From t = 1 s to the end of simulation

**Table 5**
A comparative study between the proposed optimal PR controllers with their HCs and the previously introduced controllers in the literatures.

| Controller type | Conventional PI (Ortega Gonzalez et al., 2014) | Adaptive PI (Elnady and AlShabi, 2019) | PI Plus HCs (Ortega Gonzalez et al., 2014) | PI-P plus HCs (Ortega Gonzalez et al., 2014) | Single input interval type-2 fuzzy integral (Gheisarnejad et al., 2020) | Virtual impedance and voltage compensation scheme (Baghaee et al., 2018) | Harmonic droop compensation (Moussa et al., 2019) | PR plus HCs (Vasquez et al., 2013) | Proposed optimal PR plus HCs |
|---|---|---|---|---|---|---|---|---|---|
| $THD_v$ (%) | 8.8 | 1.6 | 5.2 | 2.2 | 1.66 | 4.5 | 1.88 | 0.63 | 0.19 |

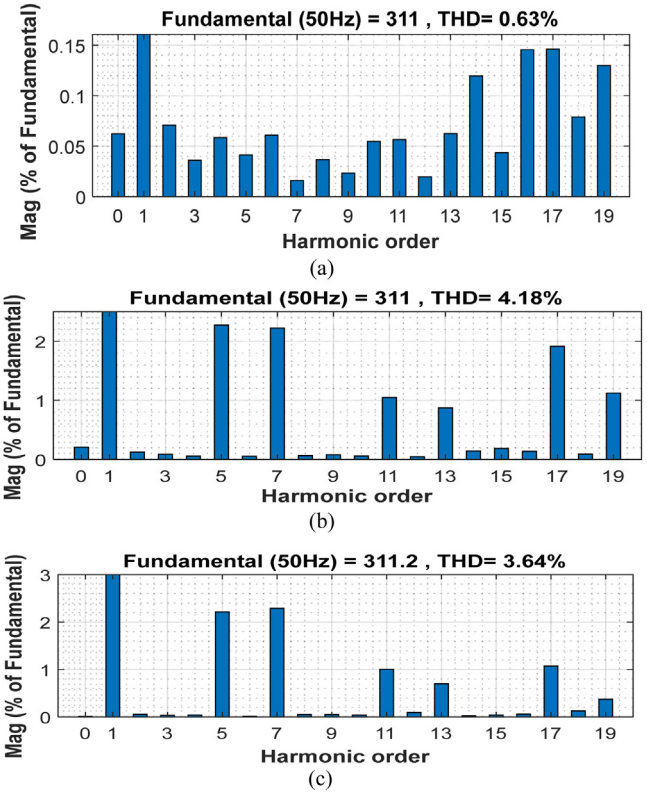


**Fig. 14.** Harmonics spectrum of the output voltage during linear, nonlinear and composite loads in the case of the voltage and current PR controllers without HCs (a) linear load; (b) nonlinear load; (c) composite load.

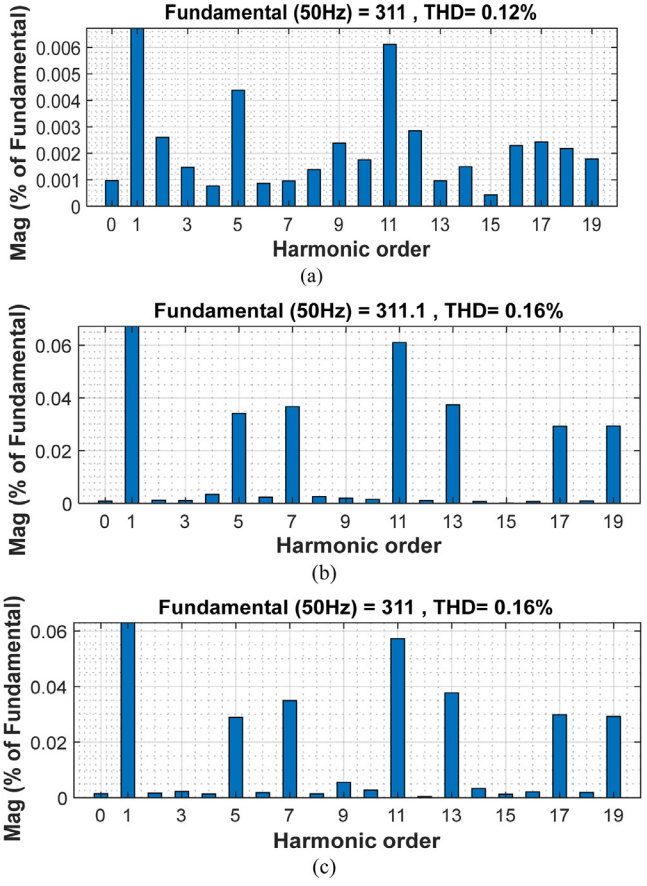


**Fig. 15.** Harmonics spectrum of the output voltage during linear, nonlinear and composite loads in the case of the proposed voltage and current PR controllers plus their HCs (a) linear load; (b) nonlinear load; (c) composite load.

time, the first grid-supporting VSI is suddenly tripped, the output active/reactive power and current of it becomes zero while those of the second inverter are doubled to compensate the interrupted amounts of the first inverter. The continuity of power supply to the connected load is maintained throughout only one grid-supporting VSI which is alone able to keep the system stability and regulate the microgrid's frequency and voltage. This result indicates that the microgrid system has high reliability and flexibility.

## 7. Conclusion

This paper has introduced new optimal design guidelines of both the PR controllers along with additional HCs and the PI controllers for three-layer cascaded control implemented on grid-supporting VSIs-based AC microgrid. The three-layer cascaded control approach is carried out in stationary $\alpha\beta$-frame, and comprised of the PCL, SCL and synchronization control level. The design procedures were conducted throughout two stages. The first stage was applied to the PCL to optimally adjust the parameters of its PR controllers along with additional HCs. In this stage, the optimization constraints/objectives aimed to improve the quality of the microgrid's output power represented in minimizing the voltage's harmonics and THD and eliminating the tracking errors for the voltage, current and frequency of the PCL. However, the second stage was employed for the SCL and the synchronization control level to appropriately design their PI controllers' coefficients. The goals of optimization in this stage were to remove the differences in voltage amplitude, frequency and phase angle between the microgrid and the external power grid, and also to reduce the overshoot/undershoot, settling time and steady-state error for the voltage and frequency of the SCL. The two stages are based on a new hybrid optimization algorithm between the HHO and PSO algorithms, namely H-HHOPSO. The suggested microgrid system, based on optimal controllers and HCs, has been modeled and simulated in a MATLAB environment to confirm the effectiveness of the proposed control approach. For the PCL, the performance of proposed H-HHOPSO-based voltage/current PR controllers with additional HCs was evaluated

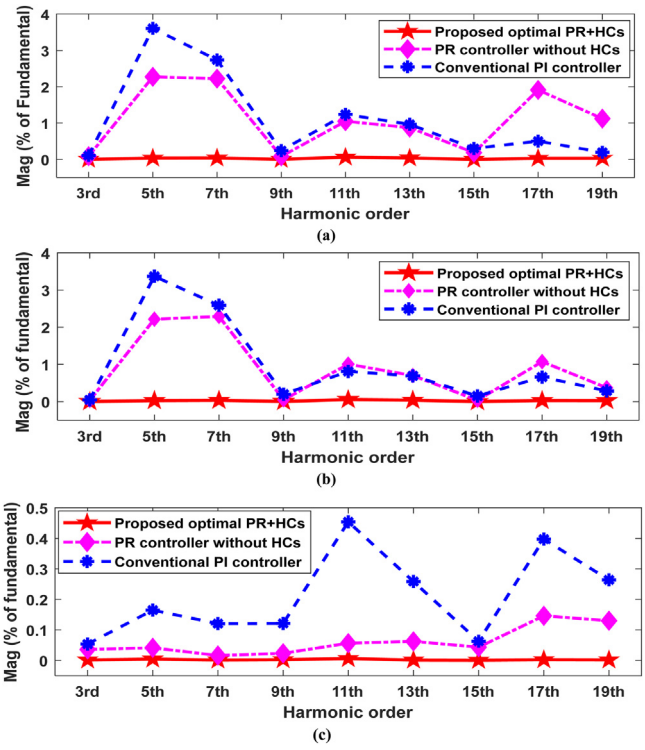


**Fig. 16.** Comparative graph of individual harmonic magnitudes between the proposed optimal PR controller plus its HCs, PR controllers without HCs, and conventional PI controller under different types of load (a) Nonlinear load (b) Linear plus nonlinear load (c) Linear load.

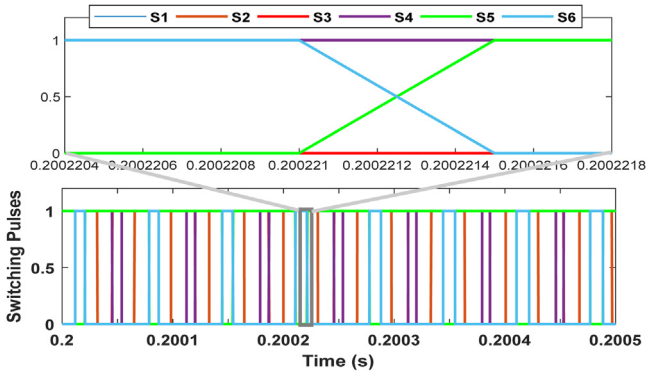


**Fig. 17.** Six switching pulses for grid-supporting inverter in the case of H-HHOPSO algorithm.

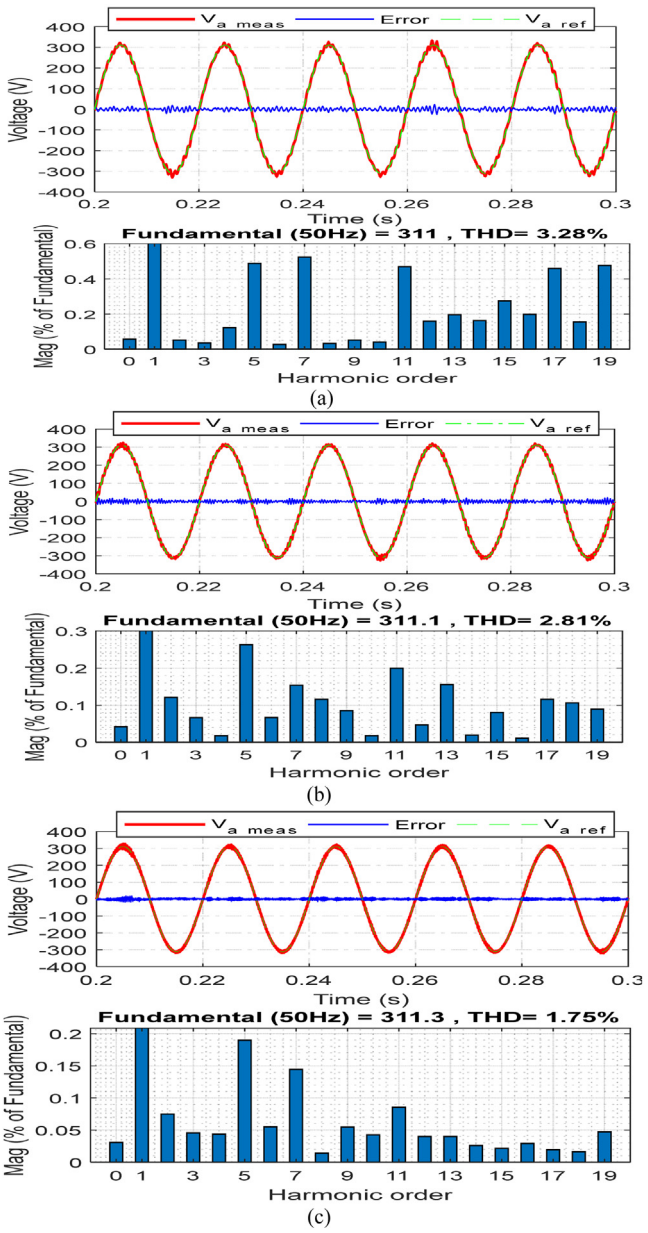


**Fig. 18.** Harmonics spectrum of the output voltage during nonlinear load in the cases of PSO, GWO and HHO-based voltage and current PR controllers with their HCs (a) PSO (b) GWO (c) HHO.

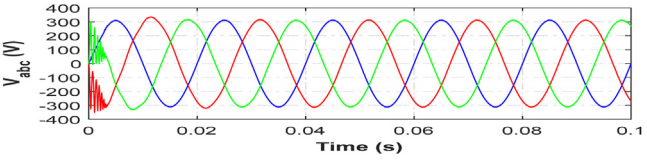


**Fig. 19.** The microgrid voltage during nonlinear loads in case of using the optimal current/voltage PR controllers with HCs.

according to IET/IEEE harmonic standards and compared with the conventional PI controllers, and also compared with PSO, GWO and HHO-based PR controllers along with additional HCs. It was noticed that the THD of the microgrid's output voltage under nonlinear load decreased from 5.23% to 4.18% to 3.28% to 2.81% to 1.75% to 0.16% in the cases of conventional PI voltage/current controllers, PR controllers without additional HCs, PSO-based PR controllers with HCs, GWO-based PR controllers with HCs, HHO-based PR controllers with HCs and H-HHOPSO-based PR controllers with HCs, respectively. It can be concluded that the proposed optimal controllers and HCs have a superior performance in minimizing both individual harmonic amplitudes and THD of the microgrid's output voltage. Moreover, they have a high tracking behavior for the references of voltage, current and frequency with the minimum values of oscillations. Additionally, the synchronization process between the external main grid and the microgrid is achieved fast and accurately with acceptable insignificant differences in voltage, frequency and phase angle. Furthermore, the active/reactive power-sharing is appropriately

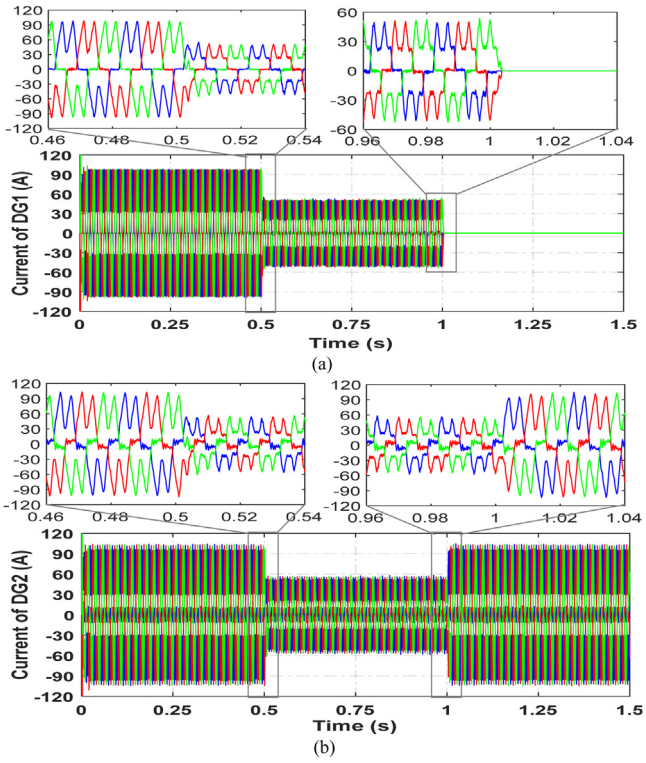


**Fig. 20.** The waveforms of output currents for the two paralleled grid-supporting inverters sharing the two nonlinear loads via the droop control methodology (a) DG1; (b) DG2.

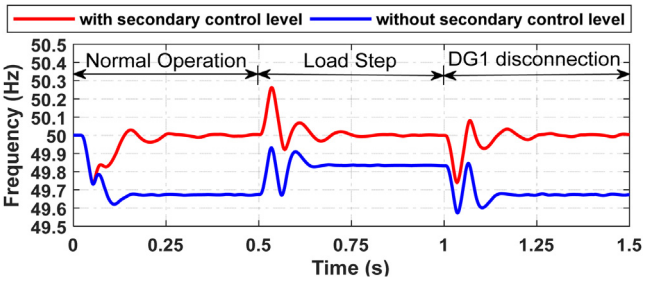


**Fig. 21.** The microgrid's frequency with and without secondary control.

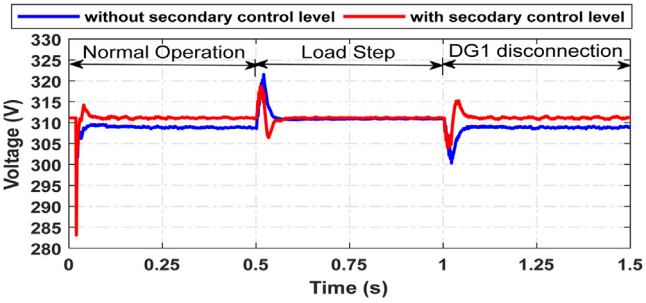


**Fig. 22.** The microgrid's voltage amplitude with and without secondary control.

realized among the parallel grid-supporting VSIs. It can be concluded that the proposed optimal controllers and HCs have a superior performance in minimizing both individual harmonic amplitudes and THD of the microgrid's output voltage.

Our future work will be extended in this research area to test the effectiveness of the proposed optimal controllers and HCs

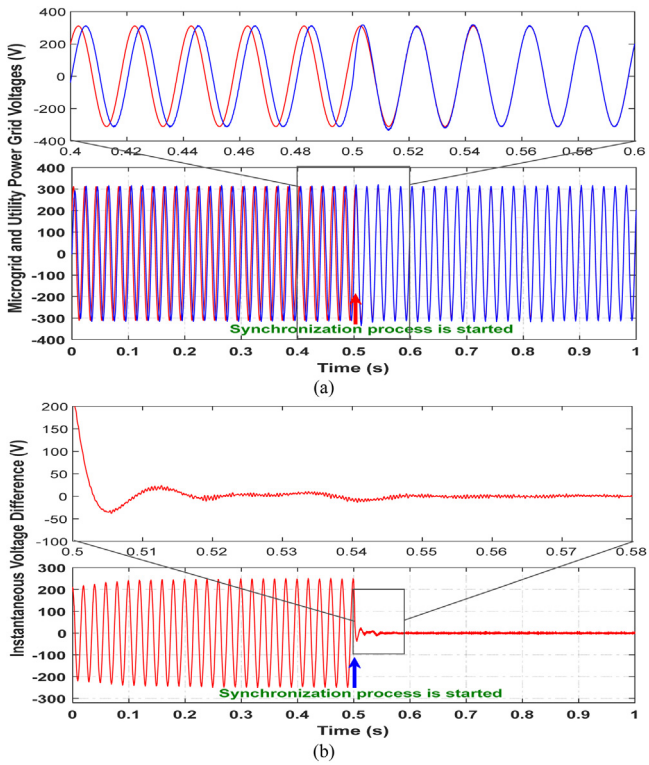


**Fig. 23.** The achievement of the synchronization procedure between the external main grid and the microgrid (a) External main grid and microgrid voltage during synchronization process (b) difference error of synchronization.

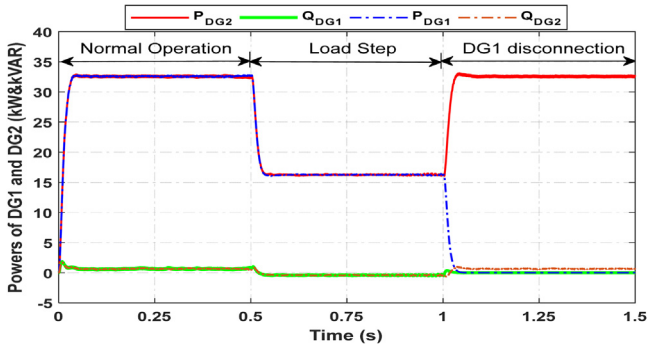


**Fig. 24.** The active/reactive power-sharing between the two grid-supporting VSIs.

under the unbalanced loads and voltage flickers. Moreover, our future work will employ these proposed optimal controllers with their HCs in AC microgrid architecture including multiple micro-sources such as PV panels, wind turbines, batteries and fuel cells. Furthermore, in the future work, the challenge represented in the complexity of experimental validation for the proposed system will be overcome using low cost hardware-in-the-loop testbed.

## CRediT authorship contribution statement

**Mohamed A. Ebrahim:** Conceptualization, Data curation, Formal analysis, Writing – original draft, Writing – review & editing. **Beshoy Abdou Aziz:** Conceptualization, Data curation, Formal analysis, Writing – original draft, Writing – review & editing. **Maged N.F. Nashed:** Conceptualization, Data curation, Formal analysis, Writing – original draft, Writing – review & editing. **F.A. Osman:** Conceptualization, Data curation, Formal analysis, Writing – original draft, Writing – review & editing.

## Declaration of competing interest

The authors declare that they have no known competing financial interests or personal relationships that could have appeared to influence the work reported in this paper.

## References


Andishgar, M.H., Gholipour, E., Hooshmand, R.A., 2017. An overview of control approaches of inverter-based microgrids in islanding mode of operation. Renew. Sustain. Energy Rev. 80, 1043–1060.

Baghaee, H.R., Mirsalim, M., Gharehpetan, G.B., Talebi, H.A., 2018. Nonlinear load sharing and voltage compensation of microgrids based on harmonic power-flow calculations using radial basis function neural networks. IEEE Syst. J. 12 (3), 2749–2759.

Bidram, A., Davoudi, A., 2012. Hierarchical structure of microgrids control system. IEEE Trans. Smart Grid 3 (4), 1963–1976.

Ebrahim, M.A., Ayoub, B.A.A., Nashed, M.N.F., Osman, F.A.M., 2021. A novel hybrid-HHOPSO algorithm based optimal compensators of four-layer cascaded control for a new structurally modified AC microgrid. IEEE Access 9, 4008–4037.

Ebrahim, M.A., Fattah, R.M.A., Saied, E.M.M., Maksoud, S.M.A., Khashab, H.E., 2020. Real-time implementation of self-adaptive salp swarm optimization-based microgrid droop control. IEEE Access 8, 185738–185751.

Elnady, A., AlShabi, M., 2019. Operation of parallel inverters in microgrid using new adaptive PI controllers based on least mean fourth technique. Math. Probl. Eng..

Farrokhabadi, M., Cañizares, C.A., Simpson-Porco, J.W., Nasr, E., Fan, L., 2020. Microgrid stability definitions, analysis, and examples. IEEE Trans. Power Syst. 35 (1), 13–29.

Gao, T., Lin, Y., Chen, D., Xiao, L., 2020. A novel active damping control based on grid-side current feedback for LCL-filter active power filter. Energy Rep. 6 (Supplement 9), 1318–1324.

Gheisarnejad, M., Mohammadi-Moghadam, H., Boudjadar, J., Khooban, M.H., 2020. Active power sharing and frequency recovery control in an islanded microgrid with nonlinear load and nondispatchable DG. IEEE Syst. J. 14 (1), 1058–1068.

Golsorkhi, M.S., Savaghebi, M., Lu, D.D., Guerrero, J.M., Vasquez, J.C., 2017. A GPS-based control framework for accurate current sharing and power quality improvement in microgrids. IEEE Trans. Power Electron. 32 (7), 5675–5687.

Guerrero, M., Chandorkar, M., Lee, T., Loh, P.C., 2013. Advanced control architectures for intelligent microgrids—Part I: Decentralized and hierarchical control. IEEE Trans. Ind. Electron. 60 (4), 1254–1262.

Guerrero, J.M., Vasquez, J.C., Matas, J., de Vicuna, L.G., Castilla, M., 2011. Hierarchical control of droop-controlled AC and DC microgrids—A general approach toward standardization. IEEE Trans. Ind. Electron. 58 (1), 158–172.

Gui, Y., Wei, B., Li, M., Guerrero, J.M., Vasquez, J.C., 2018. Passivity-based coordinated control for islanded AC microgrid. Appl. Energy 229, 551–561.

Guo, W., Mu, L., 2016. Control principles of micro-source inverters used in microgrid. Prot. Control Mod. Power Syst. 1 (1), 1–7.

Han, Y., Shen, P., Zhao, X., Guerrero, J.M., 2017. Control strategies for islanded microgrid using enhanced hierarchical control structure with multiple current-loop damping schemes. IEEE Trans. Smart Grid 8 (3), 1139–1153.

Hashempour, M.M., Savaghebi, M., Vasquez, J.C., Guerrero, J.M., 2016. A control architecture to coordinate distributed generators and active power filters coexisting in a microgrid. IEEE Trans. Smart Grid 7 (5), 2325–2336.

He, J., Li, Y.W., 2013. Hybrid voltage and current control approach for DG-grid interfacing converters with LCL filters. IEEE Trans. Ind. Electron. 60 (5), 1797–1809.

He, J., Li, Y.W., Blaabjerg, F., 2015. An enhanced islanding microgrid reactive power, imbalance power, and harmonic power sharing scheme. IEEE Trans. Power Electron. 30 (6), 3389–3401.

Heidari, A.A., Mirjalili, S., Faris, H., Aljarah, I., Mafarja, M., Chen, H., 2019. Harris hawks optimization: Algorithm and applications. Future Gener. Comput. Syst. 97, 849–872.

Hua, H., Cao, J., Yang, G., Ren, G., 2018. Voltage control for uncertain stochastic nonlinear system with application to energy internet: Non-fragile robust h∞ approach. J. Math. Anal. Appl. 463 (1), 93–110.

Hua, H., Qin, Y., He, Z., Li, L., Cao, J., 2020. Energy sharing and frequency regulation in energy internet via mixed H2/H∞ control with Markovian jump. CSEE J. Power Energy Syst..

2014. Ieee standard for interconnecting distributed resources with electric power systems - amendment 1. In: IEEE Std 1547a-2014 (Amendment To IEEE Std 1547-2003). pp. 1–16.

Jumani, T.A., Mustafa, M.W., Rasid, M.M., Mirjat, N.H., Leghari, Z.H., Saeed, M.S., 2018. Optimal voltage and frequency control of an islanded microgrid using grasshopper optimization algorithm algorithm. Energies 11 (11), 3191.

Kennedy, J., Eberhart, R.C., 1995. Particle swarm optimization. In: Proceedings of ICNN'95- International Conference on Neural Networks IV. IEEE Service Center, USA, Piscataway, NJ, pp. 1942–1948.

Li, Y.W., 2009. Control and resonance damping of voltage-source and current-source converters with LC filters. IEEE Trans. Ind. Electron. 56 (5), 1511–1521.

Meng, X., Liu, J., Liu, Z., 2019. A generalized droop control for grid-supporting inverter based on comparison between traditional droop control and virtual synchronous generator control. IEEE Trans. Power Electron. 34 (6), 5416–5438.

Mirjalili, S., Mirjalili, S.M., Lewis, A., 2014. Grey wolf optimizer. Adv. Eng. Softw. 69, 46–61.

Moussa, H., Martin, J.-P., Pierfederici, S., Meibody-Tabar, F., Moubayed, N., 2019. Voltage harmonic distortion compensation with nonlinear load power sharing in low-voltage islanded microgrid. Math. Comput. Simulation 158, 32–48.

Ortega Gonzalez, R., Sosa Saavedra, J.C., Carranza Castillo, O., Garcia Ortega, V., 2014. Comparison controllers for inverter operating in island mode in microgrids with linear and nonlinear loads. IEEE Lat. Amer. Trans. 12 (8), 1441–1448.

Shrivastava, S., Subudhi, B., Das, S., 2018. Distributed voltage and frequency synchronisation control scheme for islanded inverter-based microgrid. IET Smart Grid 1 (2), 48–56.

Shuvo, S., Hossain, E., Khan, Z.R., 2020. Fixed point implementation of grid tied inverter in digital signal processing controller. IEEE Access 8, 89215–89227.

Sreekumar, P., Khadkikar, V., 2016. A new virtual harmonic impedance scheme for harmonic power sharing in an islanded microgrid. IEEE Trans. Power Deliv. 31 (3), 936–945.

Sun, Y., Zhong, C., Hou, X., Yang, J., Han, H., Guerrero, J.M., 2017. Distributed cooperative synchronization strategy for multi-bus microgrids. Int. J. Electr. Power Energy Syst. 86, 18–28.

2008. Technical paper – definition of a set of requirements to generating units. UCTE.

Vasquez, J.C., Guerrero, J.M., Savaghebi, M., Eloy-Garcia, J., Teodorescu, R., 2013. Modeling, analysis, and design of stationary-reference-frame droop-controlled parallel three-phase voltage source inverters. IEEE Trans. Ind. Electron. 60 (4), 1271–1280.

Vu, T.K., Seong, S.j., 2010. Comparison of PI and PR controller based current control schemes for single-phase grid-connected PV inverter. Korea Acad. Ind. Soc. 11 (8), 2968–2974.

yan Jiang, X., He, C., Jermsittiparsert, K., 2020. Online optimal stationary reference frame controller for inverter interfaced distributed generation in a microgrid system. Energy Rep. 6, 134–145.

Yazdavar, A.H., Azzouz, M.A., El-Saadany, E.F., 2019. A novel decentralized control scheme for enhanced nonlinear load sharing and power quality in islanded microgrids. IEEE Trans. Smart Grid 10 (1), 29–39.

Zammit, D., Staines, C.S., Apap, M., Licari, J., 2017. Design of PR current control with selective harmonic compensators using matlab. J. Electr. Syst. Inf. Technol. 4 (3), 347–358.

Zhong, Q., 2013. Harmonic droop controller to reduce the voltage harmonics of inverters. IEEE Trans. Ind. Electron. 60 (3), 936–945.

Zhou, Y., Ngai-Man Ho, C., 2016. A review on microgrid architectures and control methods. In: 2016 IEEE 8th International Power Electronics and Motion Control Conference (IPEMC-ECCE Asia). pp. 3149–3156.